

Water Resources Research®

RESEARCH ARTICLE

10.1029/2022WR033195

Key Points:

- Future increases in tidal flooding enhance saltwater-freshwater mixing in coastal aquifers due to greater seawater infiltration
- Salinity dynamics is controlled by the interplay between sea level rise and long period tidal forcing at semiannual to decadal time scales
- The lunar nodal cycle controls the onset of tidal flooding-induced vertical salinization of coastal aquifers

Supporting Information:

Supporting Information may be found in the online version of this article.

Correspondence to:

J. W. Heiss,
james_heiss@uml.edu

Citation:

Heiss, J. W., Mase, B., & Shen, C. (2022). Effects of future increases in tidal flooding on salinity and groundwater dynamics in coastal aquifers. *Water Resources Research*, 58, e2022WR033195. <https://doi.org/10.1029/2022WR033195>

Received 5 JUL 2022

Accepted 8 DEC 2022

Effects of Future Increases in Tidal Flooding on Salinity and Groundwater Dynamics in Coastal Aquifers

James W. Heiss¹ , Bryce Mase¹, and Chengji Shen² 

¹Department of Environmental, Earth and Atmospheric Sciences, University of Massachusetts Lowell, Lowell, MA, USA,

²College of Harbour, Coastal and Offshore Engineering, Hohai University, Nanjing, China

Abstract Future increases in the frequency of tidal flooding due to sea level rise (SLR) are likely to affect pore water salinities in coastal aquifers. In this study, we investigate the impact of increased tidal flooding frequency on salinity and flow dynamics in coastal aquifers using numerical variable-density variably-saturated groundwater flow and salt transport models. Short (sub-daily) and long (decadal) period tides are combined with SLR projections to drive continuous 80-year models of flow and salt transport. Results show that encroaching intertidal zones lead to both periodic and long-term vertical salinization of the upper aquifer. Salinization of the upper aquifer due to tidal flooding forces the lower interface seaward, even under SLR. System dynamics are controlled by the interplay between SLR and long period tidal forcing associated with perigean spring tides and the 18.6-year lunar nodal cycle. Periodic tidal flooding substantially enhances intertidal saltwater-freshwater mixing, resulting in a 6- to 10-fold expansion of the intertidal saltwater-freshwater mixing area across SLR scenarios. The onset of the expansion coincides with extreme high water levels resulting from lunar nodal cycling of tidal constituent amplitudes. The findings are the first to demonstrate the combined effects of gradual SLR and short and long period tides on aquifer salinity distributions, and reveal competing influences of SLR on saltwater intrusion. The results are likely to have important implications for coastal ocean chemical fluxes and groundwater resources as tidal flooding intensifies worldwide.

1. Introduction

Fresh submarine groundwater discharge (SGD) is an important source of nutrients to nearshore ecosystems (Lecher & Mackey, 2018; Robinson et al., 2018) and has been linked to coastal eutrophication and algal blooms (Lee et al., 2010; Paerl, 1997), hypoxia (Guo et al., 2020), and stressed flora (Kwon et al., 2017) and fauna (Charbonnier, Anschutz, et al., 2016). Prior to discharge, nutrient-enriched fresh groundwater in intertidal aquifers can undergo biogeochemical processes that moderate chemical and carbon fluxes to the coastal ocean (Ahrens et al., 2020; Kroeger & Charette, 2008; Liu et al., 2021). The biogeochemical reactions along discharging flow paths are maintained by the supply of marine-derived dissolved and particulate organic carbon and other reactive constituents that infiltrate the shoreface due to tidal action (Kim et al., 2020; Seidel et al., 2015). Thus, tides are a key factor affecting coastal chemical budgets through their influence on the chemical composition of SGD. With the Intergovernmental Panel on Climate Change projecting global mean sea level to rise between 0.43 and 0.84 m by 2100 (Oppenheimer et al., 2019), it is critical to understand the impacts of encroaching intertidal zones and associated periodic tidal inundation on coastal groundwater dynamics to anticipate future changes to chemical loads to coastal water bodies.

The number of studies investigating flow and pore water geochemistry in coastal groundwater systems has risen over the past two decades (Kim & Heiss, 2021). Studies have characterized spatial distributions of oxygen (Charbonnier, Lavesque, et al., 2016), nutrients (Kroeger & Charette, 2008; Rakimbekova et al., 2021; Spiteri et al., 2006), silica (Ehlert et al., 2016), dissolved inorganic carbon (Kim et al., 2022; Liu et al., 2021), heavy metals (Santos et al., 2011), and combinations of redox-sensitive species (Beck et al., 2017; McAllister et al., 2015; O'Connor et al., 2018; Reckhardt et al., 2017; Schutte et al., 2018). Findings from a number of these and other studies indicate that the spatial extent and time scales of mixing between freshwater and saltwater in intertidal mixing zones (Figure 1a) strongly affects aquifer reactivity and chemical fluxes to marine ecosystems (Beck et al., 2017; Lecher & Mackey, 2018; Waska et al., 2019). Changes to the size, geometry, and location of intertidal saltwater-freshwater mixing zones caused by changes to the frequency and extent of inundating tides may therefore affect the delivery of nutrients, heavy metals, and carbon to surface water ecosystems. Additionally, a field

© 2022. The Authors.

This is an open access article under the terms of the Creative Commons Attribution-NonCommercial-NoDerivs License, which permits use and distribution in any medium, provided the original work is properly cited, the use is non-commercial and no modifications or adaptations are made.

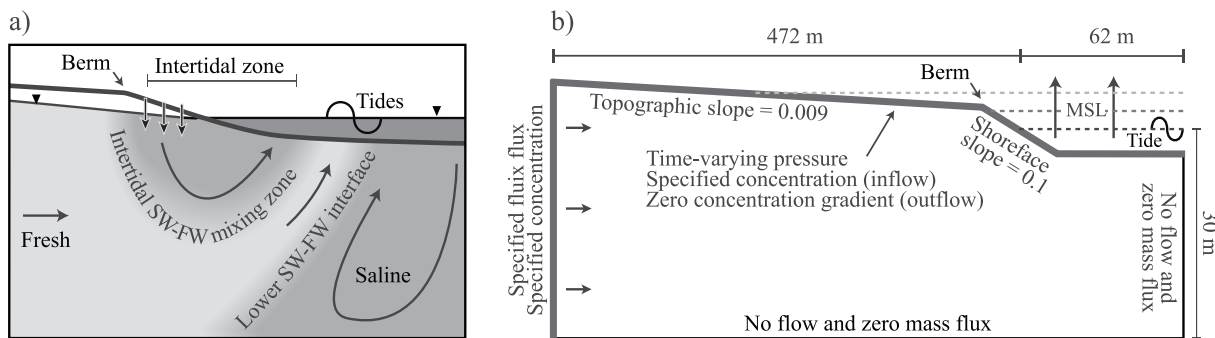


Figure 1. (a) Conceptual diagram of flow paths and saltwater-freshwater (SW-FW) mixing zones in an unconfined coastal aquifer without tidal flooding. (b) Model domain and flow and transport boundary conditions.

study by McKenzie et al. (2021) at a site influenced by wastewater found higher nutrient fluxes from the coastal aquifer during inundating king tides compared to periods with lower high tides, further suggesting that changes to the extent of inundating tides has implications for groundwater chemical fluxes to the ocean.

Seawater inundation of the land surface in coastal areas threatens fresh groundwater resources because it leads to vertical intrusion of saltwater into aquifers. Vertical salinization has received less attention in literature relative to lateral saltwater intrusion, but studies have shown that land surface inundation is a dominate control on subsurface saltwater intrusion (Ketabchi et al., 2016). For instance, rapid marine transgression can outpace inland migration of the lower saltwater-freshwater interface, resulting in seawater inundation on top of fresh groundwater and downward transport of saltwater (Kooi et al., 2000). Ferguson and Gleeson (2012) employed an analytical approach to show that low-lying coastal areas in the continental U.S. are more vulnerable to salinization from seawater inundation and infiltration from sea level rise (SLR) than lateral saltwater intrusion. Ataei-Ashtiani et al. (2013) systemically quantified the importance of land surface inundation due to SLR relative to equivalent SLR scenarios without inundation (i.e., a vertical fortified shoreline). They showed that inundation from SLR can increase intrusion of the lower interface by an order of magnitude compared to the equivalent scenario accounting only for the pressure increase at the shoreline.

In addition to SLR, episodic coastal flooding causes vertical salinization of aquifers. Vertical salinization due to discrete flooding events has been investigated in a number of studies (Gingerich et al., 2017; Mahmoodzadeh & Karamouz, 2019; Post & Houben, 2017; Yang et al., 2013, 2015, 2018, 2021; Yu et al., 2016). These investigations show that salt that accumulates in the shallow aquifer during and shortly following a coastal flooding event is later flushed out by freshwater discharging to the ocean. The discharging salt can take the form of density fingers that arise from the unstable condition of dense saltwater overlying fresh groundwater (Mahmoodzadeh & Karamouz, 2019; Yang et al., 2013). The combined and individual effects of storm surge, SLR, and storm surge return interval have also been explored (Chui & Terry, 2012; Mahmoodzadeh & Karamouz, 2019; Paldor & Michael, 2021; Storlazzi et al., 2018). Mahmoodzadeh and Karamouz (2019) performed numerical simulations for comparing subsurface salinity distributions following a surge event under instantaneous and gradual SLR. They found that storm surge under gradual SLR resulted in more realistic subsurface salinity distributions compared to the instantaneous SLR scenarios, emphasizing the importance of resolving interacting inundation mechanisms in models. Over shorter time scales, other studies have performed numerical simulations that resolve both tidal fluctuations and inundating surge events (Huizer et al., 2017; Yang et al., 2013). All of the above studies evaluated the effects of one or multiple extreme inundation events representing storm surge or tsunami, which last on the order of minutes to days with return intervals of years to decades. However, no study has examined the combined effects of gradual SLR and tidal inundation on subsurface salinity distributions. The interplay between these processes causes tidally inundated areas to gradually migrate upward and landward onto gentle sloping land surfaces, increasing the land surface area exposed to inundating tides. Unlike surge- or tsunami-induced vertical salinization where saline groundwater can flush out of the system between events, the expansion and migration of the intertidal zone due to SLR represents a continuous vertical salinization mechanism that is likely to influence the distribution and dynamics of subsurface salinity.

Sea level rise is projected to rapidly increase the frequency and severity of tidal flooding events along a majority of the U.S. coastline as local flood elevation thresholds are more frequently exceeded (Karegar et al., 2017; Moftakhar et al., 2015; Spanger-Siegfried et al., 2014; Sweet & Park, 2014; Sweet et al., 2014; Thompson et al., 2021). For instance, communities in New Jersey, Maryland, and Washington D.C. can expect the number of tidal floods each year to increase from 40 to 50 in present-day to 150–200 by 2030 (Spanger-Siegfried et al., 2014). High tide flooding can be caused by astronomical tides alone or due to a combination of astronomical tides, wind-driven water levels, and heavy precipitation. Tidal flooding has increasingly been acknowledged as a growing issue, yet to date studies have focused on surficial flooding and societal, infrastructure, and economic impacts (Burgos et al., 2018; Gold et al., 2022; Hino et al., 2019; Jacobs et al., 2018; Karegar et al., 2017; Moftakhar et al., 2015, 2017, 2018; Ray & Foster, 2016; Sweet & Park, 2014).

Interacting tidal constituents at the coastline drive the exchange of water and solutes across the aquifer-ocean interface over a range of temporal scales. Previous studies have demonstrated that di- to quarter-diurnal tidal periods and spring-neap cycles lead to dynamic intertidal pore water salinities and increase fluid and chemical exchanges across the ocean-aquifer interface (Abarca et al., 2013; Geng & Boufadel, 2017b; Heiss & Michael, 2014; Robinson, Gibbes, et al., 2007; Yu et al., 2021). Previous studies that incorporated multi-constituent tides in numerical models generally considered four to five constituents: S₂, M₂, S₁, O₁, and K₁ (Abarca et al., 2013; Geng & Boufadel, 2015; Heiss & Michael, 2014; Robinson, Gibbes, et al., 2007; Yu et al., 2019, 2021). Together, these constituents capture the bulk of tidal stage variations over diurnal to spring-neap (monthly) time scales.

The 18.6-year lunar nodal cycle can change high tide levels by 30 cm and is a major factor affecting the timing of high tide flooding (Li et al., 2021; Peng et al., 2019). Tidal flooding frequencies are strongly linked to modulations of tidal amplitude caused by the precession of the plane of the Moon's orbit, which is tilted relative to the ecliptic (Earth-Sun plane). Thus, there are two points (nodes) of intersection between the Moon's orbit and the ecliptic. The effect of a precessing Moon orbit is a precession of the nodes, which is accompanied by a change in lunar declination relative to Earth's equatorial plane. A maximum lunar declination coincides with low high tide levels and a minimum lunar declination is associated with higher high tides. In tidal predictions, the effect of the 18.6-year nodal cycle on tide levels is captured by modifying the amplitude of each tidal constituent through time. Accordingly, the frequency of tidal flooding at a specific location is controlled by the interplay between SLR increasing high tide levels above flood thresholds, and the modulation of tidal amplitudes by precession of the nodes (Thompson et al., 2021). Additionally, there are 37 harmonic constituents used by the National Oceanic and Atmospheric Administration (NOAA) in tidal predictions. The constituents undergo constructive and destructive interference across short- (sub-daily) and long- (annual) term time scales to form a complex temporal pattern of high tide levels. These constituent interferences affect the timing of coastal flooding (Eliot, 2010). Thus, SLR, lunar nodal cycling, and high- and low-frequency tides must be considered in studies aiming to better understand future changes to groundwater systems in regions prone to tidal flooding.

The objective of this study was to assess the evolution of coastal aquifers as the inundation extent and frequency of tidal flooding events increase due to SLR. NOAA's full set of tidal constituents and multiple SLR projections were used to force groundwater flow and salt transport models of a representative coastal aquifer. Model results demonstrate the combined effects of low-frequency tidal harmonics and SLR on subsurface salinity distributions and fluid exchange patterns across the aquifer-ocean interface.

2. Methods

2.1. Numerical Model and Reference Study Site

A numerical variable-density saturated-unsaturated groundwater flow and solute transport model was used to simulate the combined effects of multi-constituent tides and long-term SLR on aquifers that underlie areas susceptible to tidal flooding. The tidally-resolved models were run for a continuous time period of 80 years (2020–2100) to fully capture long-term salinity dynamics in aquifers influenced by an increase in the frequency and extent of tidal flooding. Model simulations were conducted using a modified version of SUTRA-MS (Hughes & Sanford, 2005) to incorporate ocean forcing. Porous flow in SUTRA-MS is solved using the Richard's equation (Richards, 1931), and the van Genuchten function (van Genuchten, 1980) is used to relate capillary pressure to sediment saturation. The storage and release of water due to sediment compressibility (Reeves et al., 2000; Wilson & Gardner, 2006) was not considered because numerical tests have shown that the effects of compressibility on

flow through tidally-influenced coastal sediments is negligible when the hydraulic conductivity is greater than 10^{-6} m/s (Xin et al., 2009). The hydraulic conductivity value used in this study ($\sim 10^{-4}$ m/s) was two orders of magnitude greater than the threshold value.

The model represented a 2-D cross-section of a generic homogeneous unconfined coastal aquifer. To provide a basis for realistic ocean forcing conditions (Section 2.2) and topography (Section 2.3), the model was constructed using the tides, SLR rate, and topographic gradient at Hampton Beach, New Hampshire, U.S.A ($42^{\circ}54'33.7''N$, $70^{\circ}48'56.7''W$). The site is located in the Gulf of Maine and experiences semidiurnal tides with a range of 2.86 m between mean lower low water (MLLW) and mean higher high water (MHHW) (NOAA tidal station 8423898, Fort Point, New Hampshire). At this site, roadways, parking lots, and storm water management systems flood during seasonal high tides without the influence of storm events (Spanger-Siegfried et al., 2014). Additionally, the number of tidal flooding events in Boston, MA, located 65 km from the Hampton site, is expected to increase 13-fold from an average of 5 events in 2022 to 65 events by 2049 owing to SLR (Ray & Foster, 2016), suggesting the nearby Hampton site will experience an increase in the number of annual tidal flooding events in the future.

2.2. Boundary Conditions

The flow boundary conditions applied to the model domain included a specified fluid flux on the landward vertical boundary, specified fluid pressure along the surface boundary, and no-flow at the bottom, seaward vertical, and non-inundated surface boundaries (Figure 1b). The flux at the landward vertical boundary was set to $1.0 \text{ m}^3/\text{d}$. A specified pressure boundary was applied to model elements that were inundated according to the tidally-varying depth of the water column. A seepage face boundary condition was implemented as a mixed boundary where saturated boundary nodes above the tide level were assigned atmospheric pressure (Dirichlet boundary), and unsaturated boundary nodes above the tide level were specified as a no-flow (Neumann boundary).

The standard set of 37 NOAA tidal constituents from the Fort Point, New Hampshire tide gauge located 21 km north of Hampton Beach were used to form the tidal signal for superposing onto published SLR projections. The constituents were used in the tidal prediction formula:

$$h_t = h_0 + \sum_{i=1}^{37} N_i A_i \cos(\omega_i t - \theta_i + e_i) + r_{\text{SLR}} t \quad (1)$$

where h_t (m) is the predicted tidal elevation at time t (hr) and h_0 (m) is the reference water level (mean sea level; MSL). For each constituent i , N is the nodal factor, A (m) is the amplitude, ω ($\omega = \frac{2\pi}{T}$) is the tidal angular frequency (deg hr^{-1}), θ (deg) is the phase, and e (deg) is the equilibrium argument. The nodal factor applies an 18.6-year modulation to each constituent amplitude. Figure 2a shows the influence of the lunar nodal cycle on the tidal range over the 80-year period considered in the models. The tide range is strongly affected by a 9 cm amplitude modulation of the M_2 constituent over the nodal cycle.

SLR was incorporated into Equation 1 as linear term r_{SLR} (m/hr) upon which the predicted tide was superposed. The Boston tide gauge (NOAA tidal station #8443970, Boston, Massachusetts) is the nearest gauge with long-term SLR projections. Based on published 2100 projections, the 50th percentile SLR rate for Boston is 0.009, 0.011, and 0.015 m/yr for representative concentration pathway (RCP) 2.6, RCP 4.5, and RCP 8.5, respectively, and represent low, moderate, and high SLR scenarios (Douglas et al., 2016). These SLR scenarios were chosen to evaluate the range of possible system responses to changes in the frequency of tidal flooding and incorporate a suite of regional and global scale processes that aggregate the individual components of sea level change. The lunar nodal cycle, short and long period tides, and SLR together generated a complex 80-year ocean water level time series with an evolving mid-tide elevation, maximum daily high tide, and monthly mean high tide level (Figures 2b–2d). The multiscale cyclic forcing heavily influenced the number of annual tidal flooding events over the 80-year period (Figures S1–S3 in Supporting Information S1).

The three water level time series were assigned as a specified pressure boundary to the aquifer-ocean interface to represent oceanic forcing from the combined effects of tides and SLR, for a total of three SLR + tide scenarios. Two additional simulations were performed; one case with tides only to isolate system response to low-frequency tides without the influence of SLR, and a second case with SLR only to separate potential effects of permanent inundation on salinity distributions. The temporal discretization in the tidal models was set to 5 min to resolve

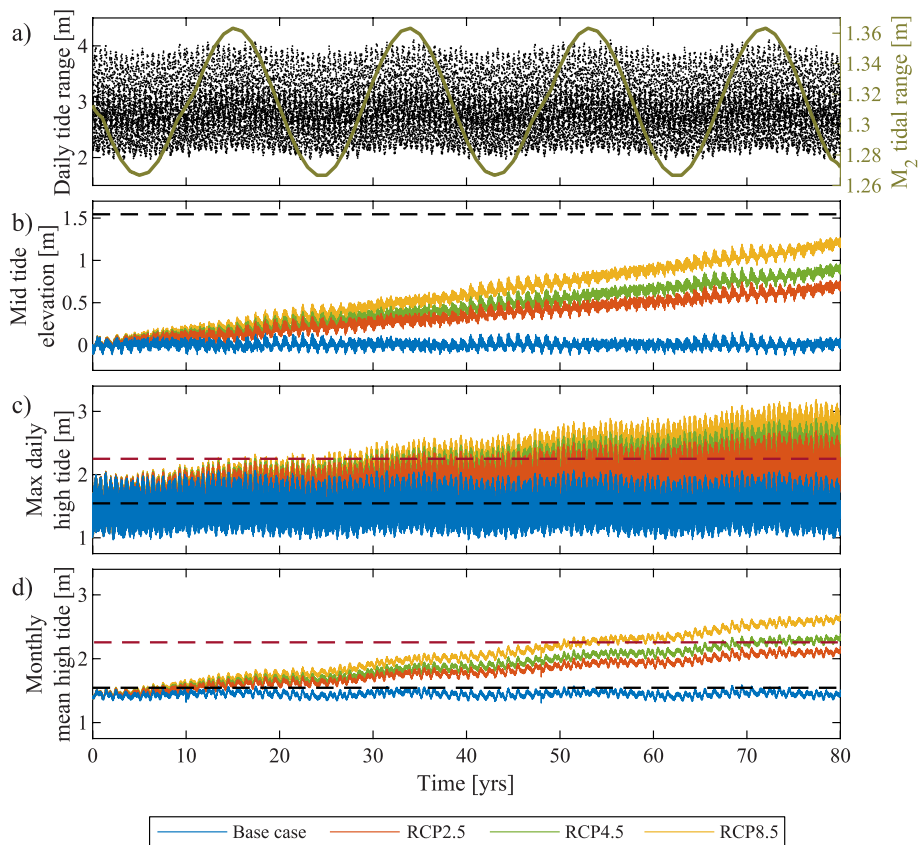


Figure 2. Tide levels for the base case and three SLR + tide scenarios over the 80-year simulation period. The black horizontal dotted line in panels (b–d) is mean higher high water. The red horizontal dotted line in panels (c–d) is the berm elevation.

tidal fluctuations over the 80-year simulation period and achieve numerical convergence. Computational and storage requirements associated with this high temporal discretization made sensitivity analysis of hydrogeological and topographic factors prohibitive. Implications related to these model limitations are discussed in Section 4.4.

The transport boundary condition across the top of the model and aquifer-ocean interface was zero-dispersive flux for outflow and a constant concentration of 35 ppt for inflow. A constant concentration of 0 ppt was assigned to the left vertical boundary. All other boundaries were set to zero mass flux.

2.3. Model Domain, Parameters, and Spatial Discretization

The model domain extended 472 m inland from the shoreline, 62 m seaward of the shoreline, and to a depth of 30 m below MSL (Figure 1b). The land surface elevation at the landward vertical boundary was set to 4.0 m, resulting in a topographic slope of 0.009 between the left boundary and berm. The selected slope represents the topographic gradient at the Hampton Beach site and is very near the median topographic gradient along the global coast (Luijendijk et al., 2020). The slope of the shoreface was set to 0.1. The berm, or the break in slope from the shoreface to the more gentle sloping land surface, was set to an elevation of 0.82 m above MHHW and is 0.14 m higher than the high tide flood threshold defined by NOAA (Sweet et al., 2014). Thus, the intertidal zone was fully contained on the shoreface at the beginning of the simulations, and the models captured the transition of a system absent of tidal flooding to one with frequent tidal inundation inland of the berm.

The model was assigned a porosity of 0.43 and a permeability of $1.2 \times 10^{-11} \text{ m}^2$, which corresponds to a hydraulic conductivity of approximately 10 m/d. Longitudinal and transverse dispersivity values were set to 0.5 and 0.05 m, respectively. The van Genuchten parameters used in the model were $S_{\text{WRES}} = 0.1$, $\alpha = 14.50 \text{ m}^{-1}$, and $n = 2.68$. A structured mesh discretized the model domain into 31,560 elements. Voss and Provost (2008) suggested mesh

discretization should satisfy numerical stability criteria defined by the Péclet number ($Pe = \frac{\Delta L}{\alpha_L} \leq 4$), where ΔL is the distance between two adjacent element faces and α_L is the longitudinal dispersivity. The maximum Pe value was 4.0, satisfying the Péclet condition. Tests were performed on grid resolution and timestep size to ensure results were independent of discretization.

2.4. Assessment Metrics

Several metrics were computed to quantify aquifer responses to tidal flooding. The cross-sectional *area of the intertidal mixing zone* is the areal sum of model elements with pore water salinity between 10% and 90% seawater, less the area of the lower saltwater-freshwater interface without tidal flooding. The *saltwater center of mass* is the cross-shore centroid location of the saltwater volume landward of the lower saltwater interface. The centroid represents the center of the circulating mass of saltwater driven by tidal flooding and was calculated from the zeroth- and first-order spatial moments:

$$x_c = \frac{M_{x,1}}{M_{x,0}} \quad (2)$$

$$z_c = \frac{M_{z,1}}{M_{z,0}} \quad (3)$$

where x_c and z_c are the x and z coordinates of the centroid, respectively, and M is the spatial moment in the x or z direction:

$$M_{s,m} = \sum_{i=1}^{N_{ele}} s_i^m c_i \quad (4)$$

where s is x or z , m is 0 or 1 representing the zeroth-order and first-order spatial moment, respectively, N_{ele} is the total number of elements in the model, and c_i is the salinity at the i th element.

Spectral analysis using Fast Fourier Transfer (FFT) was conducted to discern the dominant periods of variation in the size of the intertidal mixing zone. The analysis was limited to periods greater than one month due to data storage limitations related to the model output interval over the 80-year model runs. The FFT sampling size was 29,240 and the sampling frequency was 0.2 Hz (5 days).

3. Results

3.1. Cross-Sectional Salinity Distributions

Tidal flooding altered the distribution of fresh and saline groundwater in all SLR + tide scenarios (Figure 3). At the start of all simulations the intertidal zones were confined to the shoreface and a region of elevated salinity formed below it. The region of elevated salinity under the shoreface was separated from the lower saltwater-freshwater interface located farther seaward by a fresh groundwater discharge zone, consistent with modeled and measured salinities in other studies (Boufadel, 2000; Robinson, Li, & Barry, 2007; Vandenbohede & Lebbe, 2006). Salinity distributions in the base case were generally steady through the 80-year period (Figure 3; column 1). In models with SLR + tides, the simulated salinity distributions were unchanged for 15 years because high tide levels remained below the berm (Figure 3; columns 2–4, row 1). After 30 years, high tide levels in all three SLR + tide models exceeded the berm elevation, resulting in tidal flooding, infiltration of seawater across the land surface, and a wider intertidal saltwater-freshwater mixing zone in the shallow subsurface (Figure 3; row 2). At this stage, salinity patterns in the moderate and high SLR models reflected unstable flow conditions, which generated density instabilities and buoyancy-driven downward transport of salt fingers. The salt fingers resembled those that have been modeled in studies investigating storm surge and tidal influences on subsurface salinities (e.g., Greskowiak, 2014; Mahmoodzadeh & Karamouz, 2019; Yang et al., 2013). The salt fingers formed in all SLR + tide scenarios by year 45 and later coalesced with the lower saltwater-freshwater interface as they were transported seaward by discharging fresh groundwater (Figure 3; row 3). Groundwater salinities in these later decades became brackish to saline below an expanding intertidal zone. The continuous increase in salt mass raised pressure below the intertidal zone, which progressively forced the lower saltwater interface (>90%

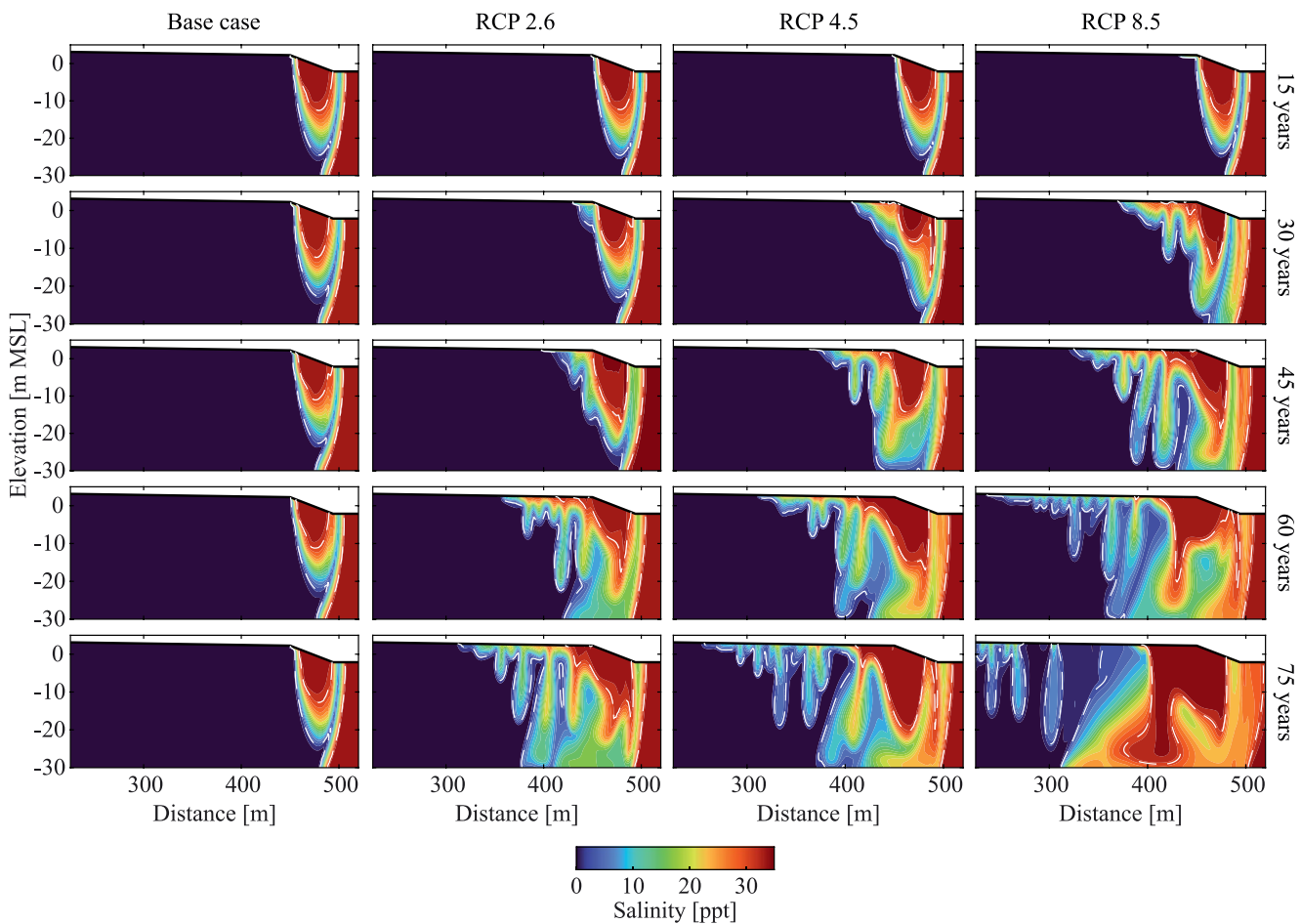


Figure 3. Salinity distributions for the base case with tides only (column 1), RCP 2.6 (column 2), RCP 4.5 (column 3), and RCP 8.5 (column 4) for year 15 (row 1), 30 years (row 2), year 45 (row 3), year 60 (row 4), and year 75 (row 5). The white contours are the 10% and 90% seawater salinity contours. Salinity varied by less than 1 ppt over individual tidal cycles, hence salinity distributions at the selected times show representative conditions.

seawater salinity) seaward in all SLR + tide scenarios despite a long-term rise in sea level (Figure 3). Comparison of salinities from the models with SLR + tides (Figure 3) to simulations with SLR alone (Figure S4 in Supporting Information S1) shows that the increased salt mass in the shallow aquifer was the result of tidal flooding from the combined effects of SLR and tides. System responses were similar across the three SLR + tide scenarios, with an expected time lag. There was a 10–15 year lag in overall salinity patterns between models with low and moderate SLR, as well as between the moderate and high SLR cases.

3.2. Water Table Salinity Dynamics

Pore water salinity along the water table increased as the high tide line encroached inland. The salinity of the water table delineates the landward and seaward boundaries of the intertidal mixing zone and cross-shore position of the fresh discharge zone and top of the lower saltwater-freshwater interface. In the base case simulation with tides only, the landward extent of the intertidal mixing zone was constant over time, while the seaward boundary oscillated 5 m over a period of 18.6 years, consistent with the length of the lunar nodal cycle (Figures 4a and 4e). The seaward expansion of the mixing zone coincided with peaks in the nodal cycle and thus large tidal amplitudes. Simulation results revealed that this seaward expansion displaced the lower saltwater-freshwater interface and fresh discharge zone seaward 5 m over the same 18.6-year nodal period.

Water table salinities for simulations with tidal flooding were markedly different from the base case simulation. In RCP 2.6, 4.5, and 8.5, inundation landward of the berm began to occur regularly in year 29, 25, and 16, respectively. This inundation and subsequent infiltration of saltwater led to a brackish water table (Figures 4b–4d),

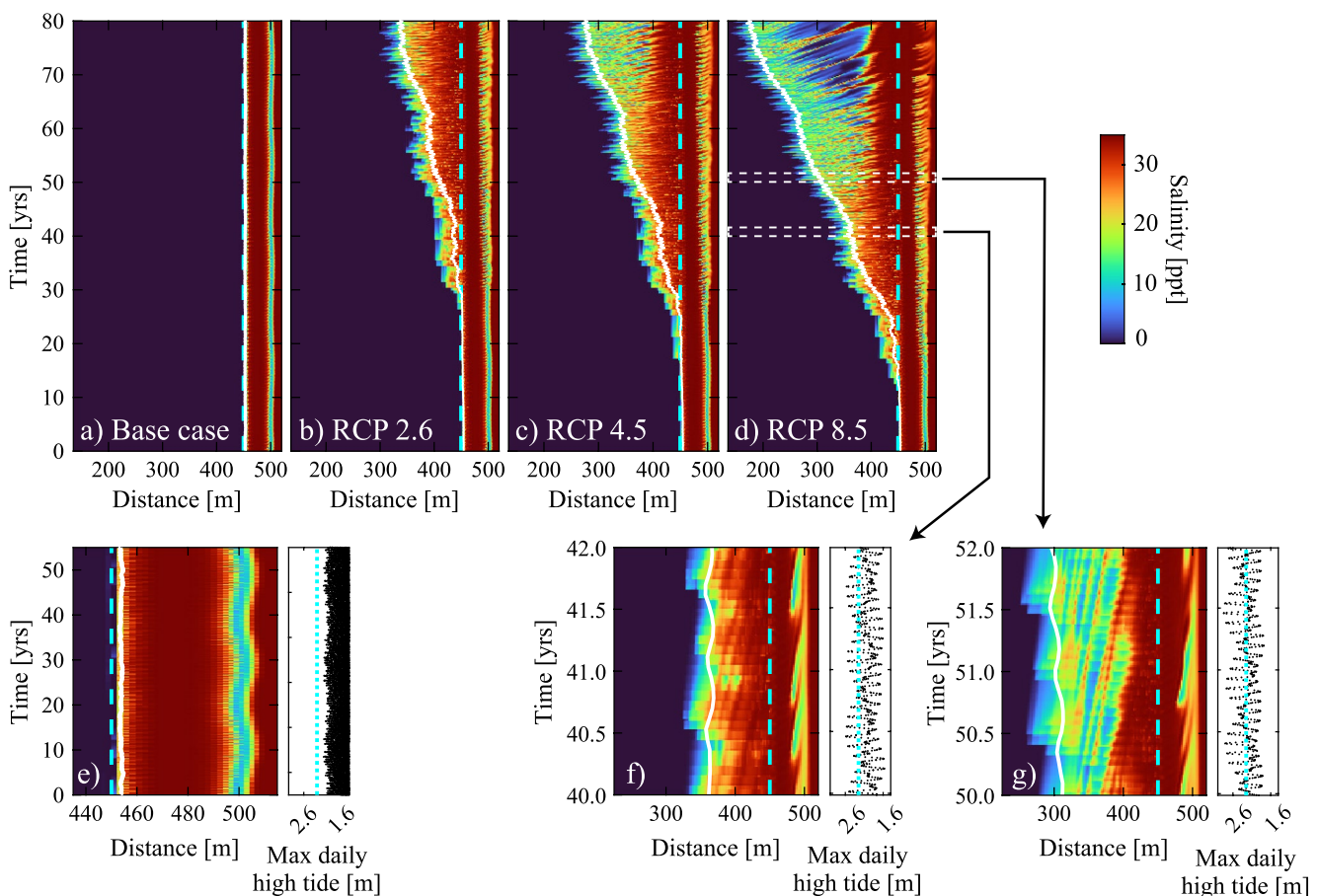


Figure 4. Salinity across the water table. Panels (a–d) show salinity for the base case (tides without SLR) and three SLR + tide scenarios over the 80-year simulation period. Panel (e) shows base case salinities identical to (a), but with a narrower x - and y -axis range to highlight cross-shore variability in the fresh discharge. Panels (f–g) are insets of RCP 8.5 at different 2-year intervals (panel e: years 40–42; panel f: years 50–52). The vertical dotted blue line is the berm. The white line is the mean annual higher high water line.

which extended up to 310 m inland of the berm for RCP 8.5. As inundation became more frequent and widespread after year 65 in RCP 4.5 and year 50 in RCP 8.5, salinity at the top of the mixing zone (i.e., water table) exhibited large spatial variability in the cross-shore, with multiple alternating pockets of saline and nearly fresh pore water (Figures 4c and 4d). The high and low salinity zones migrated seaward through time and reflect the dynamics of the top of downwelling salt fingers and rising buoyant freshwater fingers shown in Figure 3. Travel times of the fresh and saline zones, from appearance to integration with more saline groundwater farther seaward, ranged from 1 year for small fingers that formed near the berm, to up to 7 years for larger fingers that originated near the inland extent of the intertidal zone in later years. The travel times translate to horizontal finger transport velocities of 27–40 m/yr over the distances traveled.

The landward extent of the intertidal mixing zone below areas undergoing tidal flooding varied with semiannual periodicity. Figure 4f shows water table salinities and the maximum daily high tide level from year 40–42 for SLR under RCP 8.5. The landward boundary of the intertidal mixing zone oscillated 26–35 m over an approximate half-year cycle. These semiannual fluctuations, equivalent to roughly 81% of the total width of the mixing zone in the absence of tidal flooding, are owed to perigean spring tides that occur when the Earth, Moon, and Sun are in astronomical alignment, or syzygy, while the Moon is near perigee. While Earth–Moon–Sun (or Moon–Earth–Sun) alignment takes place twice a month, generating spring tides, it is only twice per year—on opposite sides of the Sun—that the alignment occurs in tandem with the Moon's perigee. Perigean spring tides are separated by a little over half a year and produce the ~0.5 year cycle of exceptionally high and inundating tides shown in Figure 4f. Water table salinity lagged 1.5–2 months behind these inundating events. The expan-

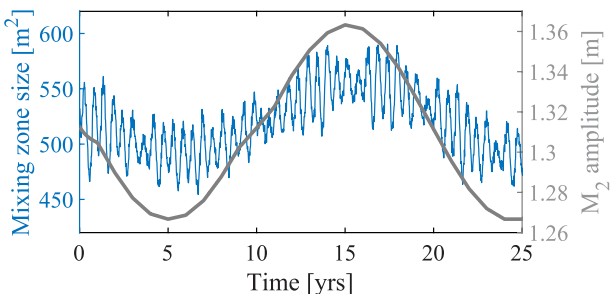


Figure 5. Cross-sectional area of the intertidal mixing zone for the base case model over 25 years (left axis), and nodal cycle modulation of the M_2 amplitude (right axis).

sion and contraction of the mixing zone from perigean spring tides was less pronounced in later decades due to the formation of salt and fresh fingers that enhanced mixing along the water table (Figure 4g).

3.3. Intertidal Mixing Zone Size

In the model case with tides only, the cross-sectional area of the intertidal mixing zone varied over semiannual to decadal timescales. The influence of perigean spring tides on the dynamics of the mixing zone size is shown in Figure 5. Greater saltwater infiltration during perigean spring tides deepened the mixing zone, which produced semiannual peaks in mixing zone area. At the decadal time scale, the mixing area was on average 520 m^2 and oscillated within a 65 m^2 range over the 18.6-year lunar nodal cycle due to the slow variation of constituent amplitudes (Figure 5).

The cross-sectional area of the intertidal mixing zone increased as tidal flooding became more frequent. In the second decade, extreme high tide levels triggered by a peak in the lunar nodal modulation (Moon's orbital declination at a minimum) resulted in the first flooding event in RCP 8.5, which initiated a growth of the mixing zone in year 15 (Figure 6). Growth was gradual from years 15–25 for RCP 8.5 because the nodal modulation was decreasing (declination of the Moon's orbital plane increasing), which damped the effects of SLR on inundation. In year 25, the nodal modulation again began to rise and high tide levels encroached inland. This coincided with rapid mixing zone expansion for RCP 8.5 and the onset of expansion for RCP 4.5 (Figure 6; top panel). The mixing zone for RCP 2.6 began to increase in size in year 30—also during a period of rising nodal modulation. Semiannual variations in mixing zone size continued for 15–30 years following the onset of inundation until unstable flow dominated, after which the mixing zone size varied more erratically. After 80 years, the area of the mixing zone for the low, moderate, and high SLR was $3,440$, $4,190$, and $5,720 \text{ m}^2$, respectively, which correspond to 6-, 7-, and 10-fold expansions of the intertidal mixing zone relative to the case with tides only (i.e.,

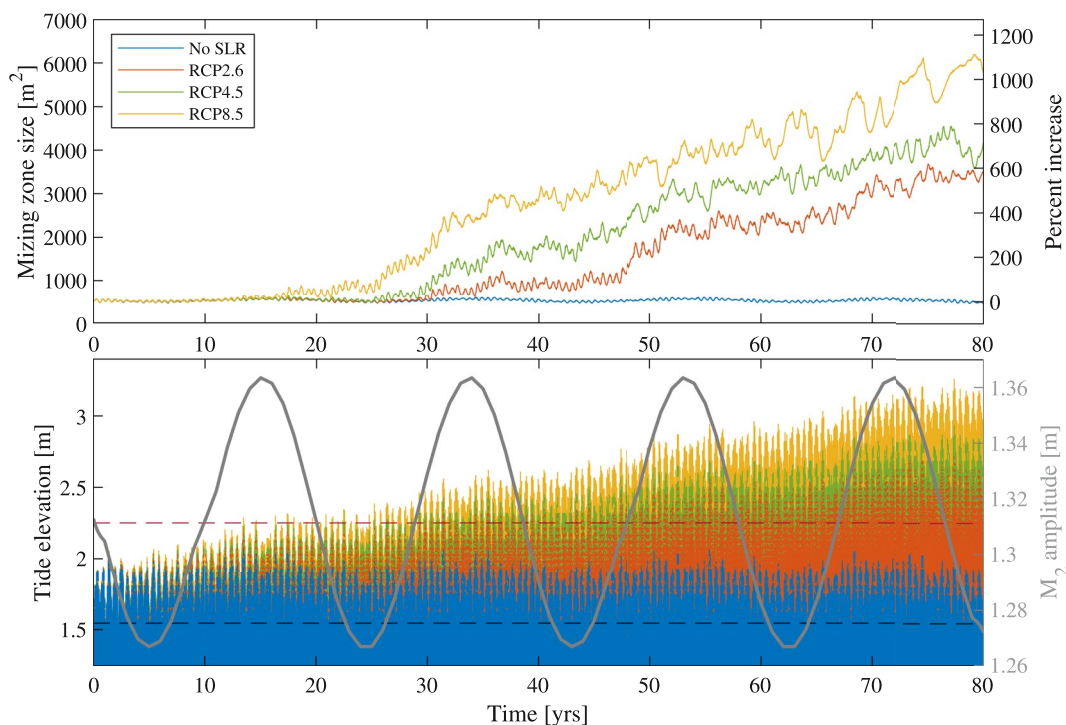


Figure 6. Top panel: Cross-sectional area of the intertidal mixing zone (left axis) and percent increase in the area of the intertidal mixing zone (right axis). Bottom panel: Tide levels (left axis) and nodal cycle modulation of the M_2 amplitude (right axis). The nodal modulation is applied to all tidal constituents; the M_2 is shown as an example. Line colors in both panels reflect the same model scenarios.

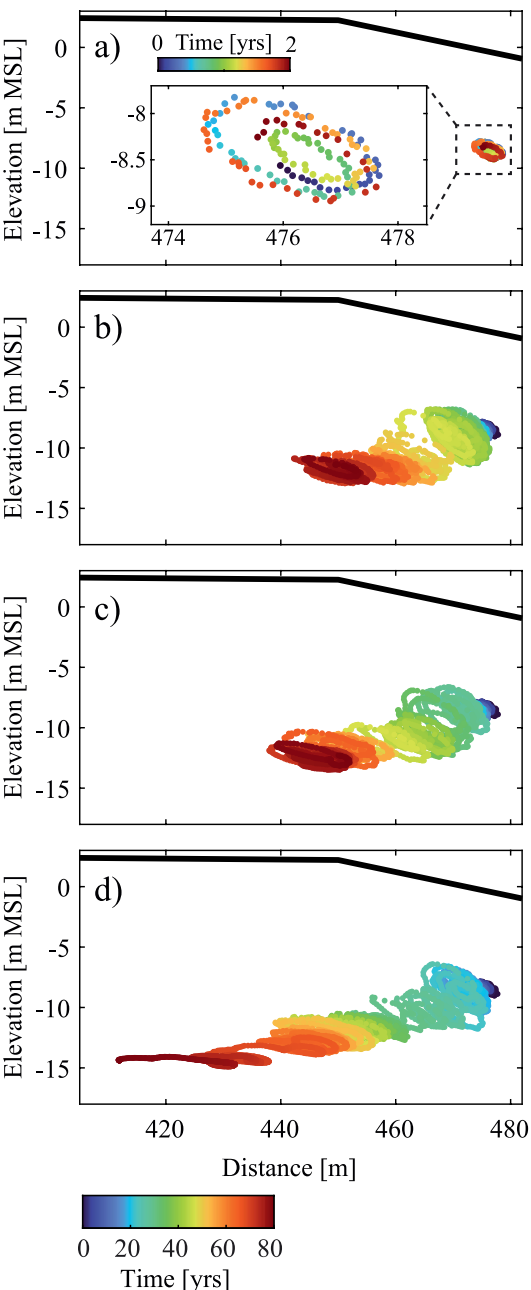


Figure 7. Center of mass of saltwater in the intertidal mixing zone for the (a) base case, (b) RCP 2.6, (c) RCP 4.5, and (d) RCP 8.5 model cases over 80 years. The inset in (a) shows the centroid for a 2-year subset.

mass under the lower shoreface out of the aquifer (Figure 9), shifting the center of mass closer to the surface. Beyond year 60 for the high SLR scenario, the slow movement of salt fingers dominated, thus the period of oscillations of the x and z centroid coordinates lengthened.

3.5. Fluid Exchange Profiles and Vertical Flow Velocities

Tidal flooding modified infiltration and discharge patterns across the aquifer-ocean interface relative to the base case. Figure 10 shows the tidally-averaged cross-shore distribution of infiltration and discharge zones in year 60.

no tidal flooding) (Figure 6; top panel). In comparison, there was negligible expansion of the mixing zone along the lower interface for model cases with SLR only (Figure S5 in Supporting Information S1). These simulation results demonstrate a strong influence of the lunar nodal cycle on both initiating and enhancing the growth of the intertidal saltwater-freshwater mixing zone across the range of SLR rates considered.

3.4. Centroid Trajectory and Movement

In the base case without tidal flooding, the trajectory of the saltwater mass centroid was affected by long-period tides. The centroid was located below the shoreface during the entire 80-year simulation (Figure 7a), consistent with the salinity distribution in Figure 3. The centroid location rotated counter-clockwise with a rotational period of approximately a half year (Figure 7a; inset). The rotational period reflects the control of perigean spring tides, whereby greater saltwater infiltration high on the shoreface during semiannual high tides shifted the mixing zone inland and pushed salt deeper into the aquifer. In response the centroid moved inland and downward before traveling seaward as high tide levels receded. The centroid in the base case model oscillated up to 3.3 m horizontally and 1.2 m vertically due to these perigee-apogee tidal cycles (Figure 8).

Centroid rotation driven by perigean spring tides was also evident in models with tidal flooding, however the circular paths were larger (Figures 7b–7d). This is because the motion was amplified by inundation and enhanced saltwater infiltration across the topographic surface landward of the berm. The centroid moved up to 8 m horizontally and 5 m vertically over perigean cycles for the three models with SLR (Figure 8). Unlike the base case, the centroid did not return to near its starting position after completing a single rotation. Instead, the net trajectory was landward due to the rise in sea level (Figures 7b–7d). The centroid moved landward 34, 38, and 64 m for the low, moderate, and high SLR rates, respectively.

The largest vertical movements of the centroid occurred in the period between the onset of flooding and 15–20 years thereafter, beginning in year 17, 26, and 30 for the high, intermediate, and low SLR rates (Figure 8). These periods correspond to a gradual transition of the groundwater system from stable to unstable conditions. For example, as Figure 3 shows for RCP 8.5, the mixing zone below the shoreface from year 15–30 evolved from a steady mass of saltwater to one with salt fingers that transported large masses of salt to the base of the aquifer. Within this quasi stable-unstable transition period, the downward penetration of salt was enhanced during inundating perigean spring tides, shifting the centroid deeper. The upward centroid trajectory during the stable-unstable transition period was driven by the interplay between saltwater infiltration during flooding and discharge of salt fingers; semiannual accumulation of salt mass in the shallow subsurface landward of the berm resulted in a buoyancy-driven overpressure that rapidly forced salt

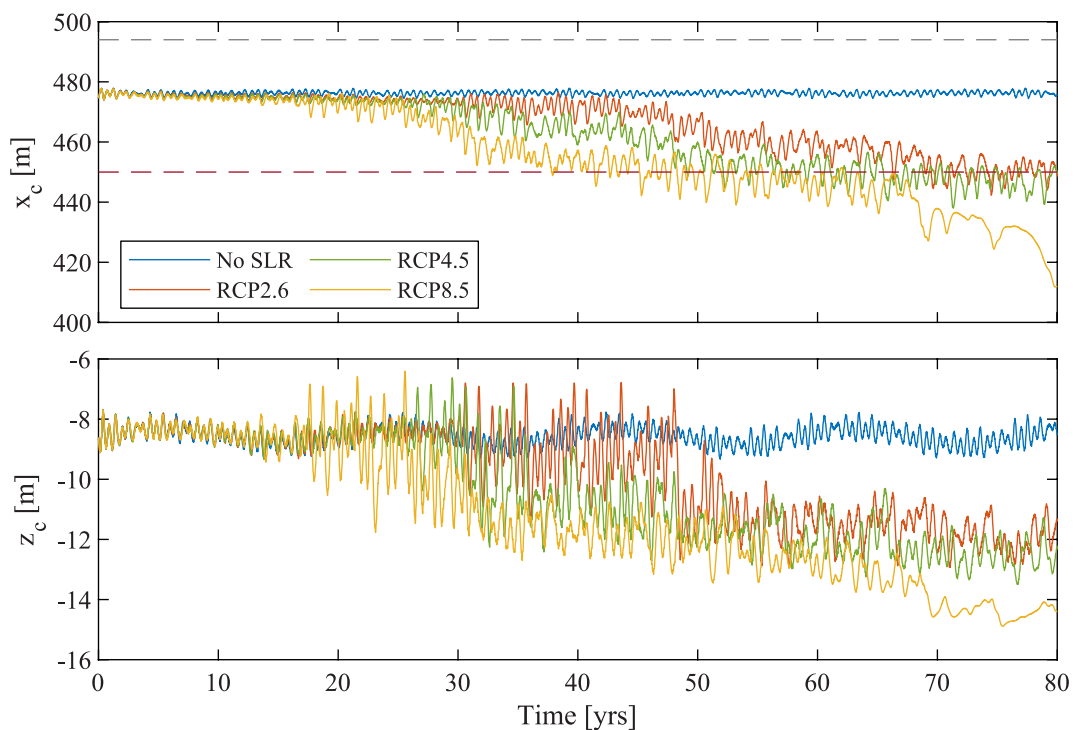


Figure 8. Movement of the x (top panel) and z (bottom panel) coordinates of the centroid of the intertidal mixing zone for the base case and three SLR + tide scenarios.

Consistent with previous studies (e.g., Robinson, Li, & Prommer, 2007), the fluid exchange profile in the base case simulation exhibited a peak in tidally-driven infiltration near the upper shoreface and a zone of focused discharge low on the shoreface (Figure 10). In this study, we show that the infiltration zone expands with a rise in sea level due to increased tidal excursion on the gentle sloping land surface. In year 60 for the low and high SLR rates, inland encroachment of the tide produced an influx area that was, respectively, 1.8 and 4.7 times wider than the area in the model case without tidal flooding.

Inland expansion of the infiltration area coincided with a landward shift of the discharge zone and a change in the shape of the discharge profile. In the base case and low SLR simulations, the discharge profile displayed a bimodal pattern that reflected discharge from two distinct and hydraulically separated flow systems; focused tidally-driven saltwater discharge formed the landward peak, and terrestrially-derived freshwater discharge formed the seaward peak (Figure 10). A bimodal discharge profile was not present in models with moderate to high SLR rates due to more unstable flow conditions that enhanced mixing near the discharge zone. We note that the infiltration and discharge rates in Figure 10 vary in time due to unstable flows and constructive and deconstructive interference between short and long period constituents that control tidal water levels. The flux profiles depicted in Figure 10 are therefore example snapshots of the spatial distribution of groundwater-surface water

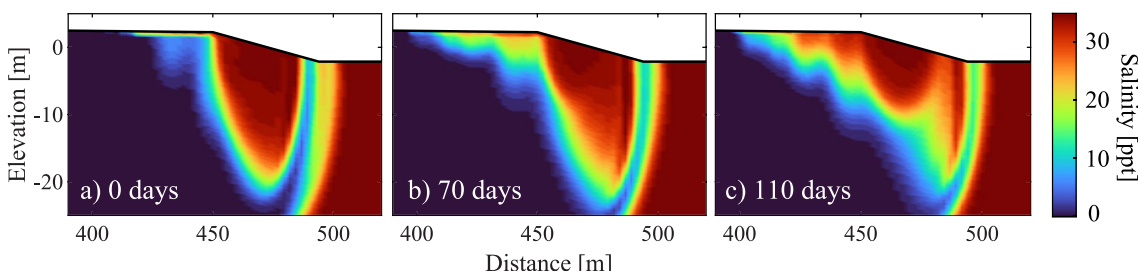


Figure 9. Salt concentration snapshots for the high (RCP 8.5) sea level rise scenario. Excess weight added to the aquifer from the vertical influx of salt mass landward of the berm during perigean spring tides forces saltwater below the shoreface out of the system. Times are relative to year 25.2.

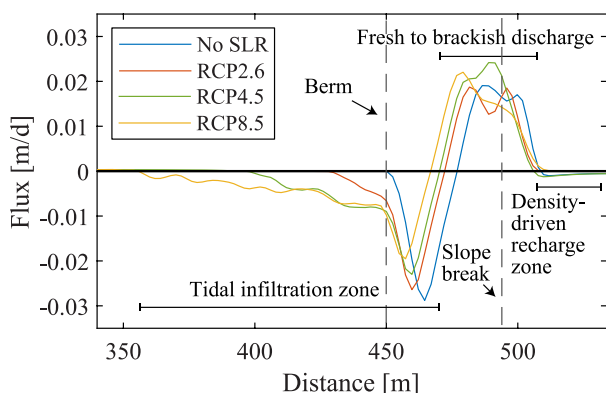


Figure 10. Tidally-averaged vertical exchange rates across the aquifer-ocean interface in year 60. Rates were calculated from the fluxes over a 14-day spring-neap cycle. Positive values denote discharge and negative values denote infiltration. The slope break is the break in slope between the shoreface and seafloor.

exchange zones. However, the spatial patterns are consistent with expanding and shifting behavior of the exchange zones at the timescale of SLR.

Downwelling and upwelling zones formed below the inundated land surface as the intertidal zone moved landward. Figure 11 shows the tidally-averaged vertical component of groundwater flow velocity from years 10–60 for the model with tides superposed on intermediate SLR. Downwelling zones that developed in years 40 and 60 overlapped with the locations of salt fingers. Downwelling and upwelling zones increased in number with the frequency of tidal flooding, and together reflected a progressively more unstable system as the intertidal zone migrated inland.

3.6. Water Table Rise

The water table landward of the berm rose due to a combination of lateral inflow from SLR and vertical infiltration from tidal flooding. The behavior of water table rise can be divided into two phases based on the onset of tidal flooding. For intermediate SLR, the water table 300 m inland of the berm increased steadily through the 80-year period due to SLR, with some tidally-driven variability at the decadal timescale owing to nodal cycling (Figure 12a). There was a similar trend 150 and 75 m inland of the berm until

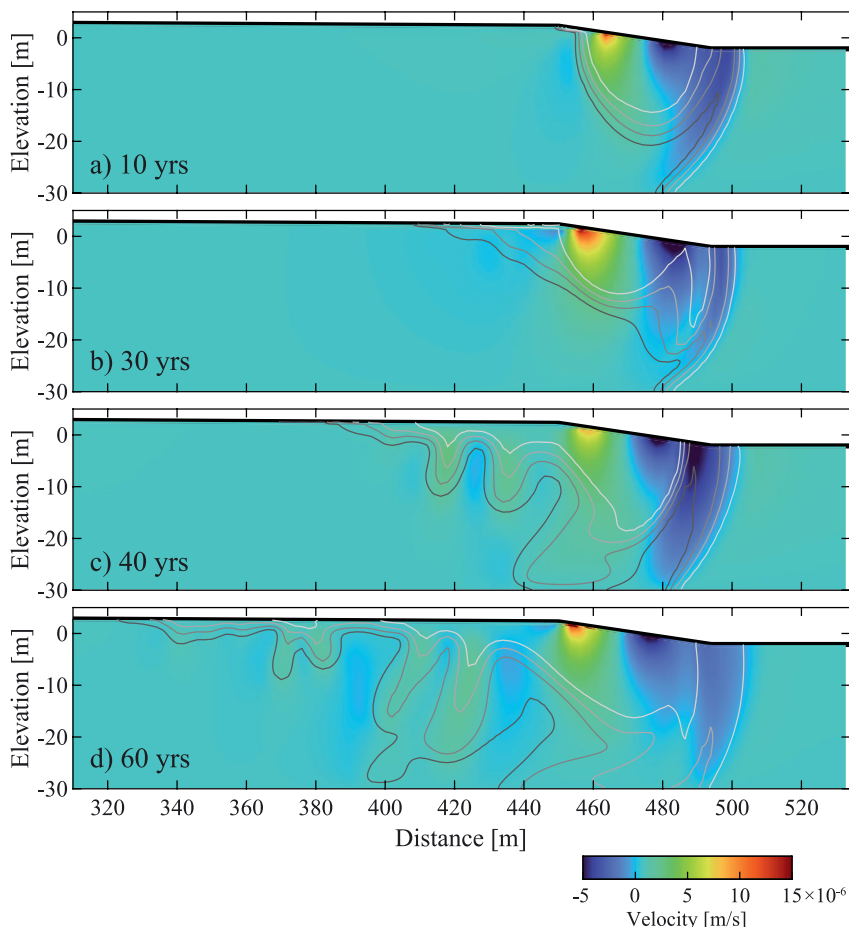


Figure 11. Tidally-averaged vertical component of groundwater flow velocity for the moderate (RCP 4.5) SLR + tide scenario in year 10, 30, 40, and 60. Positive values indicate downward flow and negative values indicate upward flow. From light gray to dark gray, the contours are the 20%, 40%, 60%, and 80% saltwater salinity contours.

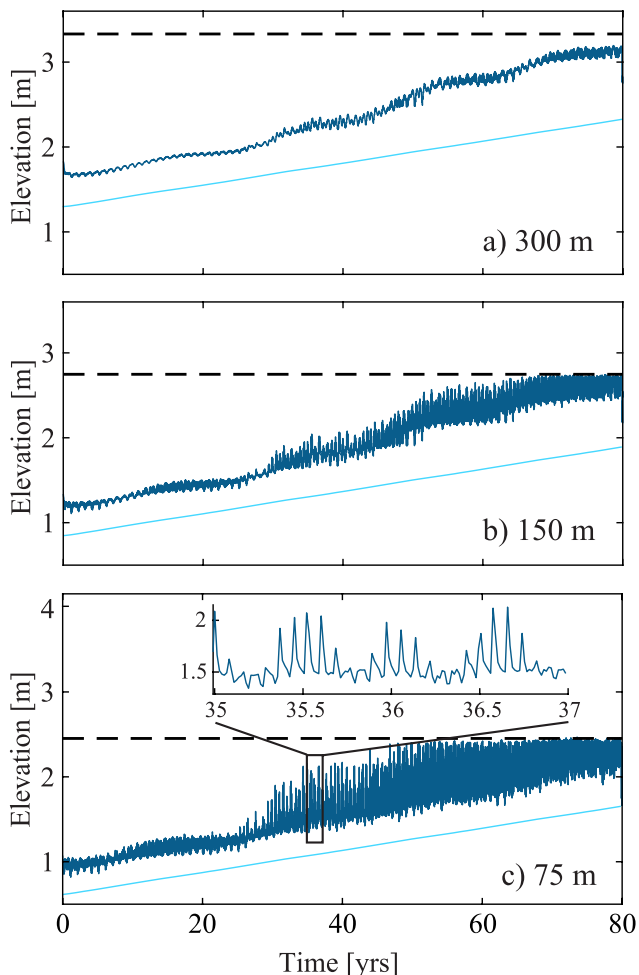


Figure 12. Water table dynamics due to increased frequency of tidal flooding (SLR + tides; dark blue) compared to sea level rise (SLR) only (light blue) at three distances inland from the berm for the moderate (RCP 4.5) SLR scenario. The black horizontal line is the land surface elevation at the respective cross-shore location.

the beginning of the third decade (Figures 12b and 12c). After approximately 30 years, the water table at these two locations oscillated 20–25 cm semi-annually due to tidal flooding, further highlighting the effects of perigean spring tides on the flow system (Figure 12c; inset). Perigean spring tides amplified the effects of monthly inundating spring tides, resulting in monthly water table fluctuations with a range of 40–50 cm. Thus, the water table fluctuated up to 75 cm over ~6 month periods due to in and out movement of long period constituent phases.

4. Discussion

A key finding of this study is the long-term expansion of the intertidal saltwater-freshwater mixing zone due to the combined effects of SLR and tides (Figure 6). From the onset of tidal flooding to year 80, the mixing zone extent increased at an average annual rate of 57, 67, and 81 m²/yr for low, intermediate, and high SLR, respectively, corresponding to an 11%–16% growth rate per year. However, this long-term expansion was punctuated by fluctuations in mixing zone size at semiannual to multidecadal time periods. Figure 13 illustrates the dominate periods of variation across these temporal scales according to the FFT spectral analysis. There are three notable peaks in the amplitude spectrum at frequencies of 1.47×10^{-4} , 5.45×10^{-4} , and 4.90×10^{-3} Hz. The frequency of 1.47×10^{-4} Hz corresponds to the 18.6-year cycling of the lunar node across the Earth-Sun plane, and the 4.90×10^{-3} Hz frequency (period = 0.56 years) is consistent with the semiannual perigean spring tide. Factors that contributed to the peak at 5.45×10^{-3} Hz (period = 5.0 years) are less clear as there is no long-period constituent or constituent interferences that result in water level oscillations at that frequency. The 5.0 year period is close to the 4.4 year modulation of high tide levels that result from perigean and declinational tidal forces going into and out of phase (Haigh et al., 2011; Pugh & Woodworth, 2014). The 0.6 year deviation may be due to lag effects from the episodic formation of salt fingers that affected mixing dynamics in the aquifer.

4.1. Implications for Aquifer Reactivity and Chemical Fluxes

The results of this study are likely to have implications for future chemical fluxes to the coastal ocean. In shallow coastal aquifers, mixing between fresh and saline groundwater drives biogeochemical reactions that are an important control on the fate and fluxes of solutes in SGD, including nutrients (Charette & Sholkovitz, 2002; Kroeger & Charette, 2008; Roy et al., 2011), mercury (Bone et al., 2007), and inorganic (Kim et al., 2022) and organic carbon (McDonough et al., 2022). Owing to the critical role of intertidal saltwater-freshwater mixing zones in affecting geochemical speciation of coastal pore water, the simulated 6- to 10-fold increase in the size of the intertidal mixing zone over the 80-year simulation period would likely substantially alter the fate of many of these nutrient, heavy metal, and carbon species in discharging groundwater through enhanced pore water reactivity. For instance, the inland encroachment of the infiltration zone will introduce marine-derived DOC, dissolved oxygen, sulfate, and other reactive species into the aquifer landward of present-day intertidal mixing zones. These compounds and elements will intercept seaward-flowing fresh groundwater earlier along freshwater flow paths. Increased solute contact time combined with enhanced mixing of these dissimilar groundwater masses is likely

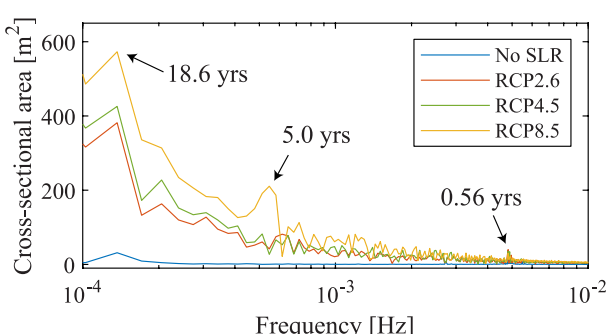


Figure 13. Amplitude spectrum of changes to the size of the intertidal mixing zone.

to enhance microbially-mediated chemical transformations, such as denitrification (Anwar et al., 2014; Heiss et al., 2017; Spiteri, Slomp, Charette, et al., 2008; Spiteri, Slomp, Tuncay, & Meile, 2008), and affect chemical loads to the coastal ocean.

The long-term increase in mixing zone size was nonlinear and fluctuated in response to half-year perigean spring tides and the 18.6-year nodal cycle (Figure 10). Temporal changes to aquifer reactivity due to the combined effects of SLR and low-frequency tidal forcing are likely similarly dynamic across these timescales as reaction zones expand, contract, and migrate with spatiotemporal changes to the subsurface intertidal mixing zone. Thus, the results provide insight into potential future occurrences of low-frequency cyclic variations in chemical delivery to the coastal ocean.

4.2. Implications for Coastal Infrastructure

Periodic vertical infiltration of saltwater across previously non-inundated land surfaces may have implications for the structural integrity of subsurface coastal infrastructure. Following the 24 June 2021 collapse of the Champlain Towers South condominium in Miami, Florida, questions were raised about potential impacts of subsurface saltwater intrusion from SLR and tidal flooding on the integrity of the building's underground foundation (Joseph et al., 2021; Parkinson, 2021). Model results from this study show that for the generic model setup considered, even infrequent tidal flooding can increase pore water salinities in the shallow subsurface due to vertical salinization. Additionally, tidally-driven water table fluctuations can increase oxygen delivery to the saturated zone (Barnes et al., 2019), which may elevate pore water dissolved oxygen concentrations near the land surface as tidally-varying water tables rise with sea level. In coastal areas, saltwater intrusion and the presence of oxygen in pore water create conditions that accelerate corrosion and decrease service life of subsurface infrastructure (Tansel & Zhang, 2022). Thus, it is recommended that coastal managers, engineers, and practitioners begin to consider these emerging risks in climate change vulnerability assessments and mitigation strategies.

4.3. Implications for Groundwater Resources

The simulation results demonstrate the importance of considering multiscale tidal forcing with SLR when evaluating aquifer vulnerability to salinization due to land surface inundation. This is evident by the controlling influence of the 18.6-year nodal cycle on the onset of vertical salinization from tidal flooding. Additionally, long period tides produce a complex pattern of ocean water levels that lead to semiannual variability in inundation extent and salinization (Figure 4). Therefore, not accounting for the combined effects of nodal cycling and long period tides will reduce the predictive ability of site-specific models that account for SLR alone.

This study also shows that the addition of salt mass below an expanding intertidal zone can increase pressures that force the lower interface seaward, even under long-term SLR. Paldor and Michael (2021) recently identified a similar offshore movement of the lower interface due to vertical salinization induced by storm surge without SLR. Our models show for the first time that an increase in pressure from vertical salinization caused by tidal flooding is a greater control on the horizontal position of the lower interface than the pressure increase in the subtidal zone from SLR. This indicates that wells screened in the deeper aquifer near tidal flooding zones may be less vulnerable to lateral saltwater contamination than suggested by the landward movement of the shoreline. Further, in areas that are projected to experience an increase in tidal flooding, deep wells that are presently contaminated by lateral intrusion due to SLR or pumping could potentially freshen as the lower interface is pushed seaward. These findings provide additional insight into the key role of marine inundation on controlling the degree of lateral saltwater intrusion (Ataie-Ashtiani et al., 2013; Ferguson & Gleeson, 2012).

4.4. Study Considerations

The aim of this study was to obtain a process-based understanding of the role of decadal scale increases in the frequency of tidal flooding on groundwater salinity distributions. This was achieved with tidally-resolved 80-year simulations with multiscale oceanic forcing. Computational limitations associated with the short time-steps required to resolve forcings across minute to decadal timescales prohibited analysis across parameter space, thus the findings are based on several simplifying assumptions.

The topographic slope used in the model coincided with the slope at Hampton Beach, NH, USA and is representative of the global median (Luijendijk et al., 2020). A steeper topographic slope would restrict inundation and decrease the presence of saline pore water landward of the berm, resulting in a smaller mixing zone. The topography of the shoreline would also likely vary over the 80 years due to sediment transport. However, the majority of locations with documented tidal flooding are in built or semi-built environments with natural or artificial shoreline hardening systems (Spanger-Siegfried et al., 2014), which are designed to reduce erosion. The immobile aquifer-ocean interface modeled in this study is most representative of these environments where the topographic profile is likely to remain more stable over SLR time scales.

The berm elevation was another important factor that likely influenced model results. A berm height of 2.25 m above MSL was chosen to capture the transition of the system from a stable to unstable state. This height is above the average berm elevation (2.01 m rel. MSL) in a compilation of berm heights across 20 coastlines (Booysen, 2017). Therefore, the onset of tidal flooding as modeled in this study is likely conservative, which is consistent with the already widespread occurrence of tidal flooding along the U.S. coastline (Sweet et al., 2020). A lower berm elevation would result in earlier inundation, which would increase salt mass in the aquifer earlier than simulated here. However, a sensitivity analysis to berm elevation and topographic slope would highlight competing influences, such as the combined effects of a low berm with high topographic slope.

The models did not consider changes to freshwater inflow along the left vertical boundary and its effects on the intertidal mixing zone (Fang et al., 2022) and tidally-driven water table fluctuations (Ataei-Ashtiani et al., 2001). Further, the specified flux boundary condition applied along the left vertical boundary is representative of a recharge-limited system where the unsaturated zone is thick enough to accommodate water table rise. While recharge-limited systems comprise approximately 30% of world coastlines, 70% of world coastlines are topography-limited in which water table rise is restricted by the land surface elevation (Michael et al., 2013). Investigation of the effects of increased frequency of tidal flooding in topography-limited systems necessitates a different landward boundary condition than implemented in the present study, specifically a specified head boundary. Nevertheless, topography-limited systems are more vulnerable to salinization than recharge-limited systems because the hydraulic gradient between land and sea cannot be maintained as SLRs (Ataei-Ashtiani et al., 1999; Werner & Simmons, 2009). This suggests that the expansion of the intertidal mixing zone as modeled in this study would be amplified in topography-limited systems represented with a specified head along the landward vertical boundary.

Oceanic forcing in the models accounted solely for SLR and astronomically-driven water levels. We did not consider seasonal (Pattullo et al., 1955) to decadal (Kolker & Hameed, 2007) cycles in mean sea level driven by temporal variability in ocean temperature, wind dynamics, and atmospheric pressure (Gill & Niller, 1973), which could augment or suppress tidal flooding. Such sea level cycles, attributed in part to large-scale climate forcing (El Niño Southern Oscillation, North Atlantic Oscillation), have been linked to salinity dynamics in unconfined coastal aquifers (Gonnea et al., 2013). The models also omitted storm surge inundation, which can affect groundwater salinities at timescales similar to those investigated in this study (Anderson, 2002; Holt et al., 2017; Terry & Chui, 2012; Yang et al., 2013). More accurate understanding of aquifer salinity responses to future tidal flooding will require consideration of these less predictable forcings.

The hydraulic conductivity in the model was assumed homogeneous and isotropic, however heterogeneity in intertidal aquifers subjected to tides can create preferential flow paths and enhance saltwater-freshwater mixing (Geng, Boufadel, et al., 2020; Geng, Michael, et al., 2020; Heiss et al., 2020). Lastly, the models did not consider the role of evaporation on increasing pore water salinities above seawater salinity, which can affect flow and salt transport in shallow intertidal sediments (Geng & Boufadel, 2015; Geng and Boufadel 2017a; Geng et al., 2016). Despite these limitations, the simplified models captured the bulk of the physics of the long-term evolution of saltwater-freshwater mixing patterns in shallow coastal aquifers.

5. Conclusions

Variable-density variably-saturated groundwater flow and salt transport models were used to investigate salinity dynamics in coastal aquifers subjected to tidal flooding. This was achieved by forcing models with 80-year tidal water levels generated from short (sub-daily) and long-(decadal) period tides and SLR projections. We

evaluated the simulated salinity distributions in the shallow subsurface of a generic low-lying coastal region as tidally-varying water levels encroached inland. To our knowledge, the results are the first to show the long-term effects of tidal flooding on subsurface saltwater-freshwater mixing and fluid fluxes across the aquifer-ocean interface.

The study demonstrated that future increases in the frequency and extent of tidal flooding can lead to cyclic variability in subsurface salinity as well as gradual long-term salinization of shallow aquifers. The salinity dynamics were driven by the interplay between SLR and long period tidal forcing at semiannual to decadal time scales. While SLR was the primary driver of tidal flooding-induced salinization, long period tides with semiannual to decadal periods also strongly influenced subsurface salinity distributions. Inland encroachment and expansion of the intertidal zone under low to high SLR resulted in a 6- to 10-fold expansion of the intertidal saltwater-freshwater mixing area. The onset of mixing area growth and periods of enhanced mixing coincided with the modulation of tidal constituent amplitudes associated with the 18.6-year lunar nodal cycle. Over shorter timescales, perigean spring tides contributed to temporal salinity patterns with semiannual periodicity.

This study has implications for groundwater resources and future chemical fluxes to coastal ocean ecosystems. The findings suggest that the projected rapid increase in the frequency of tidal flooding along the U.S. coastline may push lower saltwater-freshwater interfaces seaward due to the vertical influx of salt mass across land surfaces. Thus, it is critical that the interplay between tides and SLR is considered when aiming to assess aquifer vulnerability to saltwater intrusion. Additionally, because saltwater-freshwater mixing is a primary control on chemical cycling and fluxes, the multifold expansion of the intertidal mixing area as modeled in this study is likely, in future decades, to substantially alter pore water geochemistry and chemical delivery to the ocean along a large proportion of the coastline.

Data Availability Statement

The data necessary to reproduce the findings of this manuscript are available on CUAHSI HydroShare (Heiss, 2022).

Acknowledgments

The authors thank Marc Walther, Behzad Ataie-Ashtiani, and an anonymous reviewer for comments and suggestions that improved this manuscript. This research was supported by the U.S. National Science Foundation Grants EAR1933058 and EAR2142830 to JH.

References

- Abarea, E., Karam, H., Hemond, H. F., & Harvey, C. F. (2013). Transient groundwater dynamics in a coastal aquifer: The effects of tides, the lunar cycle, and the beach profile. *Water Resources Research*, 49(5), 1–16. <https://doi.org/10.1002/wrcr.20075>
- Ahrens, J., Beck, M., Marchant, H. K., Ahmerkamp, S., Schnetger, B., & Brumsack, H. J. (2020). Seasonality of organic matter degradation regulates nutrient and metal net fluxes in a high energy sandy beach. *Journal of Geophysical Research: Biogeosciences*, 125(2), e2019JG005399. <https://doi.org/10.1029/2019JG005399>
- Anderson, W. P. J. (2002). Aquifer salinization from storm overwash. *Journal of Coastal Research*, 18(3), 413–420.
- Anwar, N., Robinson, C., & Barry, D. A. (2014). Influence of tides and waves on the fate of nutrients in a nearshore aquifer: Numerical simulations. *Advances in Water Resources*, 73(2014), 203–213. <https://doi.org/10.1016/j.advwatres.2014.08.015>
- Ataie-Ashtiani, B., Volker, R. E., & Lockington, D. A. (1999). Tidal effects on sea water intrusion in unconfined aquifers. *Journal of Hydrology*, 216(1–2), 17–31. [https://doi.org/10.1016/S0022-1694\(98\)00275-3](https://doi.org/10.1016/S0022-1694(98)00275-3)
- Ataie-Ashtiani, B., Volker, R. E., & Lockington, D. A. (2001). Tidal effects on groundwater dynamics in unconfined aquifers. *Hydrological Processes*, 15(4), 655–669. <https://doi.org/10.1002/hyp.183>
- Ataie-Ashtiani, B., Werner, A. D., Simmons, C. T., Morgan, L. K., & Lu, C. (2013). How important is the impact of land-surface inundation on seawater intrusion caused by sea-level rise? *Hydrogeology Journal*, 21(7), 1673–1677. <https://doi.org/10.1007/s10040-013-1021-0>
- Barnes, R. T., Sawyer, A. H., Tight, D. M., Wallace, C. D., & Hastings, M. G. (2019). Hydrogeologic controls of surface water-groundwater nitrogen dynamics within a tidal freshwater zone. *Journal of Geophysical Research: Biogeosciences*, 124(11), 3343–3355. <https://doi.org/10.1029/2019JG005164>
- Beck, M., Reckhardt, A., Amelsberg, J., Bartholomä, A., Brumsack, H. J., Cypionka, H., et al. (2017). The drivers of biogeochemistry in beach ecosystems: A cross-shore transect from the dunes to the low-water line. *Marine Chemistry*, 190, 35–50. <https://doi.org/10.1016/j.marchem.2017.01.001>
- Bone, S. E., Charette, M. A., Lamborg, C. H., & Gonreea, M. E. (2007). Has submarine groundwater discharge been overlooked as a source of mercury to coastal waters? *Environmental Science & Technology*, 41(9), 3090–3095. <https://doi.org/10.1021/es0622453>
- Booyens, Z. (2017). *Berm height at temporarily open/closed estuaries in South Africa: Analysis and predictive methods*. Stellenbosch University.
- Boufadel, M. C. (2000). A mechanistic study of nonlinear solute transport in a groundwater—Surface water system under steady state and transient hydraulic conditions. *Water Resources Research*, 36(9), 2549–2565. <https://doi.org/10.1029/2000wr900159>
- Burgos, A. G., Hamlington, B. D., Thompson, P. R., & Ray, R. D. (2018). Future nuisance flooding in Norfolk, VA, from astronomical tides and annual to decadal internal climate variability. *Geophysical Research Letters*, 45(22), 12432–12439. <https://doi.org/10.1029/2018GL079572>
- Charbonnier, C., Anschutz, P., Deflandre, B., Bujan, S., & Lecroart, P. (2016). Measuring pore water oxygen of a high-energy beach using buried probes. *Estuarine, Coastal and Shelf Science*, 179, 66–78. <https://doi.org/10.1016/j.ecss.2015.12.004>
- Charbonnier, C., Lavesque, N., Anschutz, P., Bachelet, G., & Lecroart, P. (2016). Role of macrofauna on benthic oxygen consumption in sandy sediments of a high-energy tidal beach. *Continental Shelf Research*, 120, 96–105. <https://doi.org/10.1016/j.csr.2016.03.017>

- Charette, M. A., & Sholkovitz, E. R. (2002). Oxidative precipitation of groundwater-derived ferrous iron in the subterranean estuary of a coastal bay. *Geophysical Research Letters*, 29(10), 1–4. <https://doi.org/10.1029/2001GL014512>
- Chui, T. F. M., & Terry, J. P. (2012). Modeling fresh water lens damage and recovery on atolls after storm-wave washover. *Ground Water*, 50(3), 412–420. <https://doi.org/10.1111/j.1745-6584.2011.00860.x>
- Douglas, E., Kirshen, P., Hannigan, R., Herst, R., Palardy, A., DeConto, R., & Ruth, M. (2016). *Climate change and sea level rise projections for Boston: Boston research advisory Group*. Climate Ready Boston.
- Ehlert, C., Reckhardt, A., Greskowiak, J., Liguori, B. T. P., Böning, P., Paffrath, R., et al. (2016). Transformation of silicon in a sandy beach ecosystem: Insights from stable silicon isotopes from fresh and saline groundwaters. *Chemical Geology*, 440, 207–218. <https://doi.org/10.1016/j.chemgeo.2016.07.015>
- Eliot, M. (2010). Influence of interannual tidal modulation on coastal flooding along the Western Australian coast. *Journal of Geophysical Research*, 115(C11), 11013. <https://doi.org/10.1029/2010JC006306>
- Fang, Y., Zheng, T., Guo, B., Zhan, H., Wang, H., Zheng, X., & Walther, M. (2022). Transformation in the stability of tide-induced upper saline plume driven by transient external forcing. *Water Resources Research*, 58(6), e2021WR031. <https://doi.org/10.1029/2021WR031331>
- Ferguson, G., & Gleeson, T. (2012). Vulnerability of coastal aquifers to groundwater use and climate change. *Nature Climate Change*, 2(5), 342–345. <https://doi.org/10.1038/nclimate1413>
- Geng, X., & Boufadel, M. C. (2015). Impacts of evaporation on subsurface flow and salt accumulation in a tidally influenced beach. *Water Resources Research*, 51(7), 5547–5565. <https://doi.org/10.1002/2015WR016886>
- Geng, X., & Boufadel, M. C. (2017a). The influence of evaporation and rainfall on supratidal groundwater dynamics and salinity structure in a sandy beach. *Water Resources Research*, 53(7), 6218–6238. <https://doi.org/10.1002/2016wr020344>
- Geng, X., & Boufadel, M. C. (2017b). Spectral responses of gravel beaches to tidal signals. *Scientific Reports*, 7(January), 40770. <https://doi.org/10.1038/srep40770>
- Geng, X., Boufadel, M. C., & Jackson, N. L. (2016). Evidence of salt accumulation in beach intertidal zone due to evaporation. *Scientific Reports*, 6(1), 1–5. <https://doi.org/10.1038/srep31486>
- Geng, X., Boufadel, M. C., Rajaram, H., Cui, F., Lee, K., & An, C. (2020). Numerical study of solute transport in heterogeneous beach aquifers subjected to tides. *Water Resources Research*, 56(3), 1–20. <https://doi.org/10.1029/2019WR026430>
- Geng, X., Michael, H. A., Boufadel, M. C., Molz, F. J., Gerges, F., & Lee, K. (2020). Heterogeneity affects intertidal flow topology in coastal beach aquifers. *Geophysical Research Letters*, 47(17), 1–12. <https://doi.org/10.1029/2020GL089612>
- Gill, A. E., & Niller, P. P. (1973). The theory of the seasonal variability in the ocean. In *Deep sea research and oceanographic abstracts* (Vol. 20, pp. 141–177).
- Gingerich, S. B., Voss, C. I., & Johnson, A. G. (2017). Seawater-flooding events and impact on freshwater lenses of low-lying islands: Controlling factors, basic management and mitigation. *Journal of Hydrology*, 551, 676–688. <https://doi.org/10.1016/j.jhydrol.2017.03.001>
- Gold, A. C., Brown, C. M., Thompson, S. P., & Piehler, M. F. (2022). Inundation of stormwater infrastructure is common and increases risk of flooding in coastal urban areas along the US Atlantic coast. *Earth's Future*, 10(3), 1–14. <https://doi.org/10.1029/2021EF002139>
- Gonneea, M. E., Mulligan, A. E., & Charette, M. A. (2013). Climate-driven sea level anomalies modulate coastal groundwater dynamics and discharge. *Geophysical Research Letters*, 40(11), 2701–2706. <https://doi.org/10.1002/grl.50192>
- Greskowiak, J. (2014). Tide-induced salt-fingering flow during submarine groundwater discharge. *Geophysical Research Letters*, 41(18), 6413–6419. <https://doi.org/10.1002/2014GL061184>
- Guo, X., Xu, B., Burnett, W. C., Wei, Q., Nan, H., Zhao, S., et al. (2020). Does submarine groundwater discharge contribute to summer hypoxia in the Changjiang (Yangtze) River Estuary? *Science of the Total Environment*, 719, 137450. <https://doi.org/10.1016/j.scitotenv.2020.137450>
- Haigh, I. D., Eliot, M., & Pattiaratchi, C. (2011). Global influences of the 18.61 year nodal cycle and 8.85 year cycle of lunar perigee on high tidal levels. *Journal of Geophysical Research: Oceans*, 116(6), 1–16. <https://doi.org/10.1029/2010JC006645>
- Heiss, J. W. (2022). *Effects of future increases in tidal flooding on salinity and groundwater dynamics in coastal aquifers*. HydroShare. Retrieved from <https://www.hydroshare.org/resource/cb1e4d52b44f4d9ab1187162456ba04c>
- Heiss, J. W., & Michael, H. A. (2014). Saltwater-freshwater mixing dynamics in a sandy beach aquifer over tidal, spring-neap, and seasonal cycles. *Water Resources Research*, 50(8), 6747–6766. <https://doi.org/10.1002/2014WR015574>
- Heiss, J. W., Michael, H. A., & Koneshloo, M. (2020). Denitrification hotspots in intertidal mixing zones linked to geologic heterogeneity. *Environmental Research Letters*, 15(8), 084015. <https://doi.org/10.1088/1748-9326/ab90a6>
- Heiss, J. W., Post, V. E. A., Laattoe, T., Russoinello, C. J., & Michael, H. A. (2017). Physical controls on biogeochemical processes in intertidal zones of beach aquifers. *Water Resources Research*, 53(11), 9225–9244. <https://doi.org/10.1002/2017WR021110>
- Hino, M., Belanger, S. T., Field, C. B., Davies, A. R., & Mach, K. J. (2019). High-tide flooding disrupts local economic activity. *Science Advances*, 5(2), 1–10. <https://doi.org/10.1126/sciadv.aau2736>
- Holt, T., Seibert, S. L., Greskowiak, J., Freund, H., & Massmann, G. (2017). Impact of storm tides and inundation frequency on water table salinity and vegetation on a juvenile barrier island. *Journal of Hydrology*, 554, 666–679. <https://doi.org/10.1016/j.jhydrol.2017.09.014>
- Hughes, J. D., & Sanford, W. E. (2005). SUTRA-MS a version of SUTRA modified to simulate heat and multiple-solute transport: U.S. Geological Survey open-file report 2004-1207.
- Huizer, S., Karaoulis, M. C., Oude Essink, G. H. P., & Bierkens, M. F. P. (2017). Monitoring and simulation of salinity changes in response to tide and storm surges in a sandy coastal aquifer system. *Water Resources Research*, 53(8), 6487–6509. <https://doi.org/10.1002/2016WR020339>
- Jacobs, J. M., Cattaneo, L. R., Sweet, W., & Mansfield, T. (2018). Recent and future outlooks for nuisance flooding impacts on roadways on the U.S. East Coast. *Transportation Research Record*, 2672(2), 1–10. <https://doi.org/10.1177/0361198118756366>
- Joseph, C. J., Laugisch, M., Acevedo, L., Baldonado, V., Dave, K. R., Glenny, A., et al. (2021). Final report of the Miami-Dade County grand jury (pp. 1–43).
- Karegar, M. A., Dixon, T. H., Malservisi, R., Kusche, J., & Engelhart, S. E. (2017). Nuisance flooding and relative sea-level rise: The importance of present-day land motion. *Scientific Reports*, 7(1), 11197. <https://doi.org/10.1038/s41598-017-11544-y>
- Ketabchi, H., Mahmoodzadeh, D., Ataie-Ashtiani, B., & Simmons, C. T. (2016). Sea-level rise impacts on seawater intrusion in coastal aquifers: Review and integration. *Journal of Hydrology*, 535, 235–255. <https://doi.org/10.1016/j.jhydrol.2016.01.083>
- Kim, K. H., & Heiss, J. (2021). Methods in capturing the spatiotemporal dynamics of flow and biogeochemical reactivity in sandy beach aquifers: A review. *Water*, 13(6), 782. <https://doi.org/10.3390/w13060782>
- Kim, K. H., Heiss, J. W., Geng, X., & Michael, H. A. (2020). Modeling hydrologic controls on particulate organic carbon contributions to beach aquifer biogeochemical reactivity. *Water Resources Research*, 56(10), 1–17. <https://doi.org/10.1029/2020WR027306>
- Kim, K. H., Heiss, J. W., Michael, H. A., Ullman, W. J., & Cai, W.-J. (2022). Seasonal and spatial production patterns of dissolved inorganic carbon and total alkalinity in a shallow beach aquifer. *Frontiers in Marine Science*, 9(6), 1–12. <https://doi.org/10.3389/fmars.2022.856281>

- Kolker, A. S., & Hameed, S. (2007). Meteorologically driven trends in sea level rise. *Geophysical Research Letters*, 34(23), 23616. <https://doi.org/10.1029/2007GL031814>
- Kooi, H., Groen, J., & Leijnse, A. (2000). Modes of seawater intrusion during transgressions. *Water Resources Research*, 36(12), 3581–3589. <https://doi.org/10.1029/2000WR900243>
- Kroeger, K. D., & Charette, M. A. (2008). Nitrogen biogeochemistry of submarine groundwater discharge. *Limnology & Oceanography*, 53(3), 1025–1039. <https://doi.org/10.4319/lo.2008.53.3.1025>
- Kwon, H. K., Kang, H., Oh, Y. H., Park, S. R., & Kim, G. (2017). Green tide development associated with submarine groundwater discharge in a coastal harbor, Jeju, Korea. *Scientific Reports*, 7(1), 1–9. <https://doi.org/10.1038/s41598-017-06711-0>
- Lecher, A., & Mackey, K. (2018). Synthesizing the effects of submarine groundwater discharge on marine biota. *Hydrology*, 5(4), 60. <https://doi.org/10.3390/hydrology5040060>
- Lee, Y., Kim, G., Lim, W., & Hwang, D. (2010). A relationship between submarine groundwater-borne nutrients traced by Ra isotopes and the intensity of dinoflagellate red-tides occurring in the southern sea of Korea. *Limnology & Oceanography*, 55(1), 1–10. <https://doi.org/10.4319/lo.2010.55.1.0001>
- Li, S., Wahl, T., Talke, S. A., Jay, D. A., Orton, P. M., Liang, X., et al. (2021). Evolving tides aggravate nuisance flooding along the U.S. coastline. *Science Advances*, 7(10), 1–10. <https://doi.org/10.1126/sciadv.abe2412>
- Liu, Y., Jiao, J. J., Liang, W., Santos, I. R., Kuang, X., & Robinson, C. (2021). Inorganic carbon and alkalinity biogeochemistry and fluxes in an intertidal beach aquifer: Implications for ocean acidification. *Journal of Hydrology*, 595(January), 126036. <https://doi.org/10.1016/j.jhydrol.2021.126036>
- Luijendijk, E., Gleeson, T., & Moosdorf, N. (2020). Fresh groundwater discharge insignificant for the world's oceans but important for coastal ecosystems. *Nature Communications*, 11(1), 1260. <https://doi.org/10.1038/s41467-020-15064-8>
- Mahmoodzadeh, D., & Karamouz, M. (2019). Seawater intrusion in heterogeneous coastal aquifers under flooding events. *Journal of Hydrology*, 568(November 2018), 1118–1130. <https://doi.org/10.1016/j.jhydrol.2018.11.012>
- McAllister, S., Barnett, J. M., Heiss, J. W., Findlay, A. J., Macdonald, D. J., Dow, C. L., et al. (2015). Dynamic hydrologic and biogeochemical processes drive microbially enhanced iron and sulfur cycling within the intertidal mixing zone of a beach aquifer. *Limnology & Oceanography*, 60(1), 329–345. <https://doi.org/10.1111/lio.10029>
- McDonough, L. K., Andersen, M. S., Behnke, M. I., Rutledge, H., Oudone, P., Meredith, K., et al. (2022). A new conceptual framework for the transformation of groundwater dissolved organic matter. *Nature Communications*, 13(1), 1–11. <https://doi.org/10.1038/s41467-022-29711-9>
- McKenzie, T., Habel, S., & Dulai, H. (2021). Sea-level rise drives wastewater leakage to coastal waters and storm drains. *Limnology and Oceanography Letters*, 6(3), 154–163. <https://doi.org/10.1002/lo2.10186>
- Michael, H. A., Russoiello, C. J., & Byron, L. (2013). Global assessment of vulnerability to sea-level rise in topography-limited and recharge-limited coastal groundwater systems. *Water Resources Research*, 49(4), 2228–2240. <https://doi.org/10.1002/wrcr.20213>
- Moftakhar, H. R., AghaKouchak, A., Sanders, B. F., Allaire, M., & Matthew, R. A. (2018). What is nuisance flooding? Defining and monitoring an emerging challenge. *Water Resources Research*, 54(7), 4218–4227. <https://doi.org/10.1029/2018WR022828>
- Moftakhar, H. R., AghaKouchak, A., Sanders, B. F., Feldman, D. L., Sweet, W., Matthew, R. A., & Luke, A. (2015). Increased nuisance flooding due to sea-level rise: Past and future. *Geophysical Research Letters*, 42(22), 9846–9852. <https://doi.org/10.1002/2015GL066072>
- Moftakhar, H. R., AghaKouchak, A., Sanders, B. F., & Matthew, R. A. (2017). Cumulative hazard: The case of nuisance flooding. *Earth's Future*, 5(2), 214–223. <https://doi.org/10.1002/2016EF000494>
- O'Connor, A. E., Krask, J. L., Canuel, E. A., & Beck, A. J. (2018). Seasonality of major redox constituents in a shallow subterranean estuary. *Geochimica et Cosmochimica Acta*, 224, 344–361. <https://doi.org/10.1016/j.gca.2017.10.013>
- Oppenheimer, M., Glavovic, B. C., Hinkel, J., van de Wal, R., Magnan, A. K., Abd-Elgawad, A., et al. (2019). Sea Level rise and implications for low-lying islands, coasts and communities. In *The ocean and cryosphere in a changing climate* (pp. 321–446). Cambridge University Press. <https://doi.org/10.1017/9781009157964.006>
- Pael, H. W. (1997). Coastal eutrophication and harmful algal blooms: Importance of atmospheric deposition and groundwater as new nitrogen and other nutrient sources. *Limnology & Oceanography*, 42(5_part_2), 1154–1165. https://doi.org/10.4319/lo.1997.42.5_part_2.1154
- Paldor, A., & Michael, H. A. (2021). Storm surges cause simultaneous salinization and freshening of coastal aquifers, exacerbated by climate change. *Water Resources Research*, 57(5), 1–14. <https://doi.org/10.1029/2020WR029213>
- Parkinson, R. W. (2021). Speculation on the role of sea-level rise in the tragic collapse of the Surfside condominium (Miami Beach, Florida USA) was a bellwether moment for coastal zone management practitioners. *Ocean & Coastal Management*, 215, 105968. <https://doi.org/10.1016/j.ocecoaman.2021.105968>
- Pattullo, J., Munk, W., Revelle, R., & Strong, E. (1955). The seasonal oscillation in sea level. *Journal of Marine Research*, 14, 88–113.
- Peng, D., Hill, E. M., Meltzner, A. J., & Switzer, A. D. (2019). Tide gauge records show that the 18.61-year nodal tidal cycle can change high water levels by up to 30 cm. *Journal of Geophysical Research: Oceans*, 124(1), 736–749. <https://doi.org/10.1029/2018JC041695>
- Post, V. E. A., & Houben, G. J. (2017). Density-driven vertical transport of saltwater through the freshwater lens on the island of Baltrum (Germany) following the 1962 storm flood. *Journal of Hydrology*, 551, 689–702. <https://doi.org/10.1016/j.jhydrol.2017.02.007>
- Pugh, D. T., & Woodworth, P. L. (2014). *Sea level science: Understanding tides, surges, tsunamis and mean sea-level changes*. Cambridge University Press.
- Rakhimbekova, S., O'Carroll, D. M., & Robinson, C. E. (2021). Factors controlling phosphorus mobility in nearshore aquifers adjacent to large lakes. *Science of the Total Environment*, 799, 149443. <https://doi.org/10.1016/j.scitotenv.2021.149443>
- Ray, R. D., & Foster, G. (2016). Future nuisance flooding at Boston caused by astronomical tides alone. *Earth's Future*, 4(12), 578–587. <https://doi.org/10.1002/2016EF000423>
- Reckhardt, A., Beck, M., Greskowiak, J., Schnetger, B., Böttcher, M. E., Gehre, M., & Brumsack, H.-J. (2017). Cycling of redox-sensitive elements in a sandy subterranean estuary of the southern North Sea. *Marine Chemistry*, 188, 6–17. <https://doi.org/10.1016/j.marchem.2016.11.003>
- Reeves, H. W., Thibodeau, P. M., Underwood, R. G., & Gardner, L. R. (2000). Incorporation of total stress changes into the ground water model SUTRA. *Ground Water*, 38(1), 89–98. <https://doi.org/10.1111/j.1745-6584.2000.tb00205.x>
- Richards, L. A. (1931). Capillary conduction of liquids through porous mediums. *Physics*, 1(5), 318–333. <https://doi.org/10.1063/1.1745010>
- Robinson, C., Gibbes, B., Carey, H., & Li, L. (2007). Salt-freshwater dynamics in a subterranean estuary over a spring-neap tidal cycle. *Journal of Geophysical Research*, 112(C9), 1–15. <https://doi.org/10.1029/2006JC003888>
- Robinson, C., Li, L., & Barry, D. A. (2007). Effect of tidal forcing on a subterranean estuary. *Advances in Water Resources*, 30(4), 851–865. <https://doi.org/10.1016/j.advwatres.2006.07.006>
- Robinson, C., Li, L., & Prommer, H. (2007). Tide-induced recirculation across the aquifer-ocean interface. *Water Resources Research*, 43(7), 1–14. <https://doi.org/10.1029/2006WR005679>

- Robinson, C., Xin, P., Santos, I. R., Charette, M. A., Li, L., & Barry, D. A. (2018). Groundwater dynamics in subterranean estuaries of coastal unconfined aquifers: Controls on submarine groundwater discharge and chemical inputs to the ocean. *Advances in Water Resources*, 115, 315–331. <https://doi.org/10.1016/j.advwatres.2017.10.041>
- Roy, M., Martin, J. B., Smith, C. G., & Cable, J. E. (2011). Reactive-transport modeling of iron diagenesis and associated organic carbon remineralization in a Florida (USA) subterranean estuary. *Earth and Planetary Science Letters*, 304(1–2), 191–201. <https://doi.org/10.1016/j.epsl.2011.02.002>
- Santos, I. R., Burnett, W. C., Misra, S., Suryaputra, I. G. N. A., Chanton, J. P., Dittmar, T., et al. (2011). Uranium and barium cycling in a salt wedge subterranean estuary: The influence of tidal pumping. *Chemical Geology*, 287(1–2), 114–123. <https://doi.org/10.1016/j.chemgeo.2011.06.005>
- Schutte, C. A., Wilson, A. M., Evans, T., Moore, W. S., & Joye, S. B. (2018). Deep oxygen penetration drives nitrification in intertidal beach sands. *Limnology & Oceanography*, 63(S1), S193–S208. <https://doi.org/10.1002/limo.10731>
- Seidel, M., Beck, M., Greskowiak, J., Riedel, T., Waska, H., Suryaputra, I. G. N. A., et al. (2015). Benthic-pelagic coupling of nutrients and dissolved organic matter composition in an intertidal sandy beach. *Marine Chemistry*, 176, 150–163. <https://doi.org/10.1016/j.marchem.2015.08.011>
- Spanger-Siegfried, E., Fitzpatrick, M., & Dahl, K. (2014). *Encroaching tides: How sea level rise and tidal flooding threaten U.S. East and Gulf coast communities over the next 30 years* (Vol. 76). Union of Concerned Scientists.
- Spiteri, C., Regnier, P., Slomp, C. P., & Charette, M. A. (2006). pH-Dependent iron oxide precipitation in a subterranean estuary. *Journal of Geochemical Exploration*, 88(1–3), 399–403. <https://doi.org/10.1016/j.gexplo.2005.08.084>
- Spiteri, C., Slomp, C. P., Charette, M. A., Tuncay, K., & Meile, C. (2008). Flow and nutrient dynamics in a subterranean estuary (Waquoit Bay, MA, USA): Field data and reactive transport modeling. *Geochimica et Cosmochimica Acta*, 72(14), 3398–3412. <https://doi.org/10.1016/j.gca.2008.04.027>
- Spiteri, C., Slomp, C. P., Tuncay, K., & Meile, C. (2008). Modeling biogeochemical processes in subterranean estuaries: Effect of flow dynamics and redox conditions on submarine groundwater discharge of nutrients. *Water Resources Research*, 44(2), W02430. <https://doi.org/10.1029/2007WR006071>
- Storlazzi, C. D., Gingerich, S. B., Van Dongeren, A., Cheriton, O. M., Swarzenski, P. W., Quataert, E., et al. (2018). Most atolls will be uninhabitable by the mid-21st century because of sea-level rise exacerbating wave-driven flooding. *Science Advances*, 4(4), 1–9. <https://doi.org/10.1126/sciadv.aap9741>
- Sweet, W., Park, J., Marra, J., Zervas, C., & Gill, S. (2014). Sea level rise and nuisance flood frequency changes around the United States NOAA technical report NOS CO-OPS 073, 58. <https://doi.org/10.13140/2.1.3900.2887>
- Sweet, W. V., Dusek, G., Carbin, G., Marra, J., Marcy, D., & Simon, S. (2020). 2019 state of U.S. high tide flooding and a 2020 outlook NOAA technical report NOS CO-OPS 092, 17.
- Sweet, W. V., & Park, J. (2014). From the extreme to the mean: Acceleration and tipping points of coastal inundation from sea level rise. *Earth's Future*, 2(12), 579–600. <https://doi.org/10.1002/2014ef000272>
- Tansel, B., & Zhang, K. (2022). Effects of saltwater intrusion and sea level rise on aging and corrosion rates of iron pipes in water distribution and wastewater collection systems in coastal areas. *Journal of Environmental Management*, 315, 115153. <https://doi.org/10.1016/j.jenvman.2022.115153>
- Terry, J. P., & Chui, T. F. M. (2012). Evaluating the fate of freshwater lenses on atoll islands after eustatic sea-level rise and cyclone-driven inundation: A modelling approach. *Global and Planetary Change*, 88–89, 76–84. <https://doi.org/10.1016/j.gloplacha.2012.03.008>
- Thompson, P. R., Widlansky, M. J., Hamlington, B. D., Merrifield, M. A., Marra, J. J., Mitchum, G. T., & Sweet, W. (2021). Rapid increases and extreme months in projections of United States high-tide flooding. *Nature Climate Change*, 11(7), 584–590. <https://doi.org/10.1038/s41558-021-01077-8>
- Vandenbohede, A., & Lebbe, L. (2006). Occurrence of salt water above fresh water in dynamic equilibrium in a coastal groundwater flow system near De Panne, Belgium. *Hydrogeology Journal*, 14(4), 462–472. <https://doi.org/10.1007/s10040-005-0446-5>
- van Genuchten, M. T. (1980). Closed-form equation for predicting the hydraulic conductivity of unsaturated soils. *Soil Science Society of America Journal*, 44(5), 892–898. <https://doi.org/10.2136/sssaj1980.03615995004400050002>
- Voss, C. I., & Provost, A. (2008). A model for saturated-unsaturated variable-density ground-water flow with solute or energy transport.
- Waska, H., Greskowiak, J., Ahrens, J., Beck, M., Ahmerkamp, S., Böning, P., et al. (2019). Spatial and temporal patterns of pore water chemistry in the inter-tidal zone of a high energy beach. *Frontiers in Marine Science*, 6, 1–16. <https://doi.org/10.3389/fmars.2019.00154>
- Werner, A. D., & Simmons, C. T. (2009). Impact of sea-level rise on sea water intrusion in coastal aquifers. *Ground Water*, 47(2), 197–204. <https://doi.org/10.1111/j.1745-6584.2008.00535.x>
- Wilson, A. M., & Gardner, L. R. (2006). Tidally driven groundwater flow and solute exchange in a marsh: Numerical simulations. *Water Resources Research*, 42(1), 1–9. <https://doi.org/10.1029/2005WR004302>
- Xin, P., Jin, G., Li, L., & Barry, D. A. (2009). Effects of crab burrows on pore water flows in salt marshes. *Advances in Water Resources*, 32(3), 439–449. <https://doi.org/10.1016/j.advwatres.2008.12.008>
- Yang, J., Graf, T., Herold, M., & Ptak, T. (2013). Modelling the effects of tides and storm surges on coastal aquifers using a coupled surface-subsurface approach. *Journal of Contaminant Hydrology*, 149, 61–75. <https://doi.org/10.1016/j.jconhyd.2013.03.002>
- Yang, J., Graf, T., & Ptak, T. (2015). Sea level rise and storm surge effects in a coastal heterogeneous aquifer: A 2D modelling study in northern Germany. *Grundwasser*, 20(1), 39–51. <https://doi.org/10.1007/s00767-014-0279-z>
- Yang, J., Shen, C., Xu, T., Xie, Y., & Lu, C. (2021). On the intrusion and recovery of ocean-sourced 3 H and aquifers considering ocean-surge inundation. *Journal of Hydrology*, 604, 127241. <https://doi.org/10.1016/j.jhydrol.2021.127241>
- Yang, J., Zhang, H., Yu, X., Graf, T., & Michael, H. A. (2018). Impact of hydrogeological factors on groundwater salinization due to ocean-surge inundation. *Advances in Water Resources*, 111(November 2017), 423–434. <https://doi.org/10.1016/j.advwatres.2017.11.017>
- Yu, X., Xin, P., Shen, C., & Li, L. (2021). Effects of multiconstituent tides on a subterranean estuary with fixed-head inland boundary. *Frontiers in Environmental Science*, 8, 599041. <https://doi.org/10.3389/fenvs.2020.599041>
- Yu, X., Xin, P., Wang, S. S. J., Shen, C., & Li, L. (2019). Effects of multi-constituent tides on a subterranean estuary. *Advances in Water Resources*, 124, 53–67. <https://doi.org/10.1016/j.advwatres.2018.12.006>
- Yu, X., Yang, J., Graf, T., Koneshloo, M., O'Neal, M. A., & Michael, H. A. (2016). Impact of topography on groundwater salinization due to ocean surge inundation. *Water Resources Research*, 52(8), 5794–5812. <https://doi.org/10.1002/2016WR018814>